Chemistry–A European Journal
Research Article
doi.org/10.1002/chem.202302354
Chemistry Europe
European Chemical Societies Publishing
www.chemeurj.org

VIP *Very Important Paper*

Special Collection

Isolation, Characterization and Reactivity of Key Intermediates Relevant to Reductive (Electro)catalysis with Cp*Rh Complexes Containing Pyridyl-MIC (MIC = Mesoionic Carbene) Ligands

Tobias Bens,[a, b] Robert R. M. Walter,[a] Julia Beerhues,[a, b, c] Clemens Lücke,[a] Julia Gabler+,[a] and Biprajit Sarkar*[a, b]

Dedicated to Julia Gabler, a wonderful soul, who departed far too soon.

In recent years, metal complexes of pyridyl-mesoionic carbene (MIC) ligands have been reported as excellent homogeneous and molecular electrocatalysts. In combination with group 9 metals, such ligands form highly active catalysts for hydrogenation/transfer hydrogenation/hydrosilylation catalysis and electrocatalysts for dihydrogen production. Despite such progress, very little is known about the structural/electrochemical/spectroscopic properties of crucial intermediates for such catalytic reactions with these ligands: solvato complexes, reduced complexes and hydridic species. We present here a comprehensive study involving the isolation, crystallographic characterization, electrochemical/spectroelectrochemical/theoretical investigations, and in-situ reactivity studies of all the aforementioned crucial intermediates involving Cp*Rh and pyridyl-MIC ligands. A detailed mechanistic study of the precatalytic activation of [RhCp*] complexes with pyridyl-MIC ligands is presented. Intriguingly, amphiphilicity of the [RhCp*]-hydride complexes was observed, displaying the substrate dependent transfer of H^+, H or H^-. To the best of our knowledge, this study is the first of its kind targeting intermediates and reactive species involving metal complexes of pyridyl-MIC ligands and investigating the interconversion amongst them.

Introduction

In the past decades, great efforts in the field of electrocatalysis have been made to design highly efficient and stable electrocatalysts to generate renewable energy-based alternatives to fossil fuels from energy-poor feedstocks into energy-rich molecular resources.[1,2,3] However, the nontrivial multi-electron transformation to the high-energetic catalytic active species is an extraordinarily complex subject.[4–7] The investigation of fragile and short-lived intermediates remains challenging and has received growing attention for the design of suitable precatalysts in the selective generation of the molecular active species.[5–7,8]

One of the most promising and well-established precatalysts in the electrochemical generation of H_2, as a suitable energy source, are the stable and facile accessible [RhCp*] (Cp* = pentamethylcyclopentadienyl) complexes with bidentate chelating ligands, such as polypyridine[2,3,9–18] or diphosphine ligands.[19] The mechanistic proposal from Kölle and Grätzel in 1987, involved a two-electron reduction from Rh(III) to Rh(I) and subsequent protonation to form the [RhCp*] hydride species, which undergoes protonolysis to H_2.[13]

Nearly 30 years later, the group of Miller and Blakemore reinvestigated the rhodium(III)hydride formation in polypyridine [RhCp*] complexes (**I**, Scheme 1, top).[11,15,16] Addition of a H^+ source to the reduced [RhCp*] complex (**II**, Scheme 1) results in the protonation of the Cp* moiety to form η^4−pentametyhlcyclopentadiene (Cp*H) capable to generate H_2. Theoretical calculations by Blakemore and Goddard, provided detailed insights into a tautomerization mechanism between the metal-bound hydride complex [HRhCp*] (**III**, Scheme 1) and the Cp* protonated [RhCp*H] (**IV**, Scheme 1)

[a] T. Bens, R. R. M. Walter, Dr. J. Beerhues, C. Lücke, J. Gabler,+ Prof. Dr. B. Sarkar
Institut für Anorganische Chemie
Universität Stuttgart
Pfaffenwaldring 55, D-70569 Stuttgart (Germany)
E-mail: biprajit.sarkar@iac.uni-stuttgart.de

[b] T. Bens, Dr. J. Beerhues, Prof. Dr. B. Sarkar
Institut für Chemie und Biochemie
Freie Universität Berlin
Fabeckstraße 34–36, 14195, Berlin (Germany)

[c] Dr. J. Beerhues
Current Address:
Institute of Chemical Research of Catalonia (ICIQ)
Barcelona Institute of Science and Technology (BIST)
Av. Paisos Catalans 16, 43007 Tarragona (Spain)

[+] deceased, January 20, 2023

Supporting information for this article is available on the WWW under https://doi.org/10.1002/chem.202302354

Special Collection This manuscript is part of a special collection on 3rd International Conference on Organometallics and Catalysis (ICOC-2023).

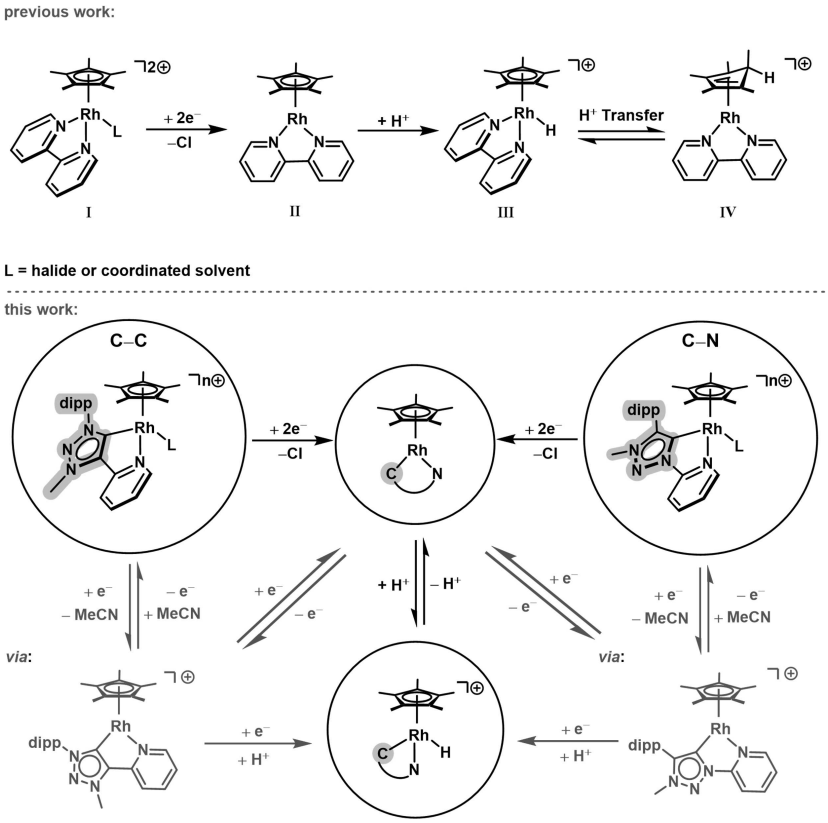

Scheme 1. Reported [RhCp*] hydride formation (top) in electrochemical H^+ reduction and presented work (bottom) for the precatalytic activation in electrocatalytically H_2 generation.

complex, as a function of the acidity of the proton source and the electronic structure of the corresponding ligands. In the presence of a weak acid, proton migration from the metal center into the Cp* ligand occurs. In agreement with the experimental finding, a stronger acid is required to evolve H_2. The direct addition of a strong acid, on the other hand, results in a rapid H_2 formation starting from the metal hydride complex, which is formed subsequently after addition to the reduced complexes.[11] In contrast, the modulation of the electronic properties by exchanging the polypyridine ligands with electron-rich 1,2-bis-(diphenylphosphino)benzene favors a metal-bound hydride complex, which show a remarkable stability.[19]

In 2015, our group reported a robust pyridyl mesoionic carbene (MIC) [CoCp*] complex for electrochemical H^+ reduction with acetic acid. The complex showed a low overpotential of 130 mV and turnover frequencies (TOF) of 4×10^2 s^{-1} with an outstanding turnover number (TON) of 650 000 at −1.54 V.[20] Additionally, Rh complexes of pyridyl-MIC ligands have been reported to be efficient hydrogenation and hydrosilylation catalysts[21] and Cp*Ir complexes with similar ligands are active transfer hydrogenation catalysts.[22] Metal complexes of pyridyl-MIC ligands were also shown to be efficient CO_2 reduction electrocatalysts.[23] For all of the aforementioned catalytic processes, the solvato, the reduced and the hydridic species are crucial intermediates. Recently, a [RhCp*] hydride complexes with a bis-NHC ligand (NHC = *N*-heterocyclic carbene) has been reported for the catalytic reduction of NAD^+ to NADH (= nicotinamide adenine dinucleotide) and crystallographically characterized.[24] However, very little information is available on their isolation and characterization, in particular with single crystal X-ray diffraction, and reactivity studies of such intermediates for complexes of pyridyl-MIC containing ligands.[25]

The ligands (**C**–**C** = pyridyl-4-triazolylidene[26] and **C**–**N** = pyridyl-1-triazolylidene)[27] presented in this work show similar overall π−acceptor properties and a highly increased overall σ−donor strength compared to the well-established bpy ligand. These properties are essential for electrocatalysis to maintain the low potential for the precatalytic activation, while increasing the electron density at the metal center to generate a highly active catalytic center.

Therefore, the high activity of the pyridyl-MIC complexes in electrocatalysis/reductive homogeneous catalysis and the aforementioned results motivated us to investigate the precatalytic activation of pyridyl-MIC containing [RhCp*] in the electrocatalytic H_2 formation with acetic acid. The combination of reaction-oriented electrochemistry with species-focused spectroscopy (spectroelectrochemistry, SEC) provides a detailed analysis of single and multiple electron-transfer processes.[4,28,29] Additionally, theoretical calculations and the isolation of highly reactive intermediates allows us to propose a mechanism for the precatalytic activation in pyridyl-MIC [RhCp*] complexes. The isolation, full characterization including single crystal X-ray diffraction, and reactivity studies of the chlorido, solvato,

hydridic and reduced complexes with the help of synthetic, crystallographic, electrochemical, spectroelectrochemical and theoretical methods are presented below.

Results and Discussion

Synthesis and Characterization

The synthesis of [Rh(**C**–**C**)Cl](PF$_6$) and [Rh(**C**–**N**)Cl](PF$_6$) was performed according to a modified silver(I)-transmetalation route reported by Bolje *et al.* for related d^6 metal complexes (**A**, Scheme 2).[30] The triazolium salt, [H(**C**–**C**)](BF$_4$) or [H(**C**–**N**)](PF$_6$), was dissolved in CH_3CN, Ag_2O was added and the suspension stirred for 3 days at room temperature under exclusion of light. After filtration and evaporation of the remaining solvent, [RhCp*Cl$_2$]$_2$ was added and dissolved in CH_2Cl_2. After three days, KPF_6 was added for salt-metathesis and the crude product was extracted with H_2O to remove the excess of salts, yielding orange crystals of [Rh(**C**–**C**)Cl](PF$_6$) (77%) or [Rh(**C**–**N**)Cl](PF$_6$) (91%) suitable for single crystal X-ray diffraction analysis (Figure 1).

To obtain the corresponding acetonitrile adducts [Rh(**C**–**C**)MeCN](PF$_6$)$_2$ and [Rh(**C**–**N**)MeCN](PF$_6$)$_2$ for detailed mechanistic studies, [Rh(**C**–**C**)Cl](PF$_6$) or [Rh(**C**–**N**)Cl](PF$_6$) was dissolved in CH_3CN and $AgPF_6$ was added (**B**, Scheme 2).[31]

The reaction mixture was stirred overnight under the exclusion of light, filtered and the concentrated solution was overlaid with *n*-hexane or first Et_2O, followed by *n*-hexane (1:1) yielding >99% of yellow crystals suitable for X-ray diffraction analysis (Figure 1).

Motivated by the work of Kölle and Blakemore, we tried to convert [Rh(**C**–**C**)Cl](PF$_6$) and [Rh(**C**–**N**)Cl](PF$_6$) with Na(Hg) in THF to access [Rh(**C**–**C**)] and [Rh(**C**–**N**)]. For these reactions, a color change from orange to deep green and purple, respectively, was observed.[17–19] However, after two hours, the reaction mixture changed to a dark brown solution, pointing to decomposition of the corresponding complexes, while some of the starting complexes remained in the crude products. Therefore, we changed our strategy using two equivalents of KC_8 in THF at −40 °C.[32] After warming up to room temperature over a two-hour period, the color-intense solution was filtered and the solvent was evaporated to complete dryness. Some drops of THF and an excess of *n*-hexane were added to the crude product, filtered and stored at −40 °C in the deep freezer for one month. We were able to collect deep purple single crystals of [Rh(**C**–**N**)] suitable for X-ray diffraction analysis (10%, Figure 1), while all crystallization attempts for [Rh(**C**–**C**)] at different temperatures and with different solvents failed.

To clarify, whether a [RhCp*] hydride complex is formed or the H^+ migrated [Rh(Cp*H)] complex, [Rh(**C**–**C**)Cl](PF$_6$) and [Rh(**C**–**N**)Cl](PF$_6$) was converted with an aqueous solution of NaOOCH/HCOOH (pH = 4.8) as hydride transferring agent, similar to a reported protocol.[15] In contrast to the direct protonation of [Rh(**C**–**C**)] and [Rh(**C**–**N**)], which did not work out, the synthesis with an aqueous solution of NaOOCH/HCOOH resulted in a clean conversion to the metal-bound hydrido complex [Rh(**C**–**C**)H](PF$_6$) and [Rh(**C**–**N**)H](PF$_6$) complexes (**D**, Scheme 2). Diffusion of *n*-hexane into a concentrated THF solution of [Rh(**C**–**N**)H](PF$_6$) yielded 43% of orange crystals suitable for X-ray diffraction analysis (Figure 1), while the

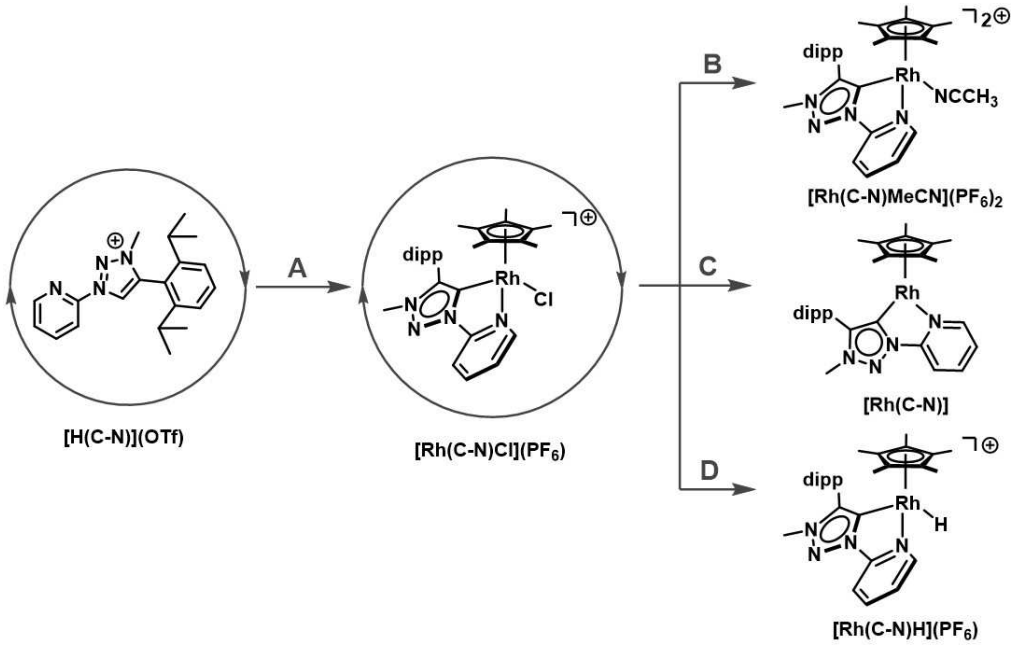

Scheme 2. Synthetic strategy for [Rh(**C**–**N**)Cl](PF$_6$), [Rh(**C**–**N**)MeCN](PF$_6$)$_2$, [Rh(**C**–**N**)] and [Rh(**C**–**N**)H](PF$_6$). Path **A**: [H(**C**–**N**)](PF$_6$), Ag_2O, CH_3CN, rt, 3 d; [RhCp*Cl$_2$]$_2$, CH_2Cl_2, rt, 3 d; KPF_6. Path **B**: [Rh(**C**–**N**)Cl](PF$_6$), $AgPF_6$, CH_3CN, rt, overnight. Path **C**: [Rh(**C**–**N**)Cl](PF$_6$), KC_8, THF, −40 °C to rt, 2 h. Path **D**: [Rh(**C**–**N**)Cl](PF$_6$), NaOOCH/HCOOH (pH = 4.8), 85 °C, 2 h. The same conditions were applied for [Rh(**C**–**C**)Cl](PF$_6$), [Rh(**C**–**C**)MeCN](PF$_6$)$_2$, [Rh(**C**–**C**)] and [Rh(**C**–**N**)H](PF$_6$), except for path **D** with an increased reaction time from 2 h to an overnight reaction.

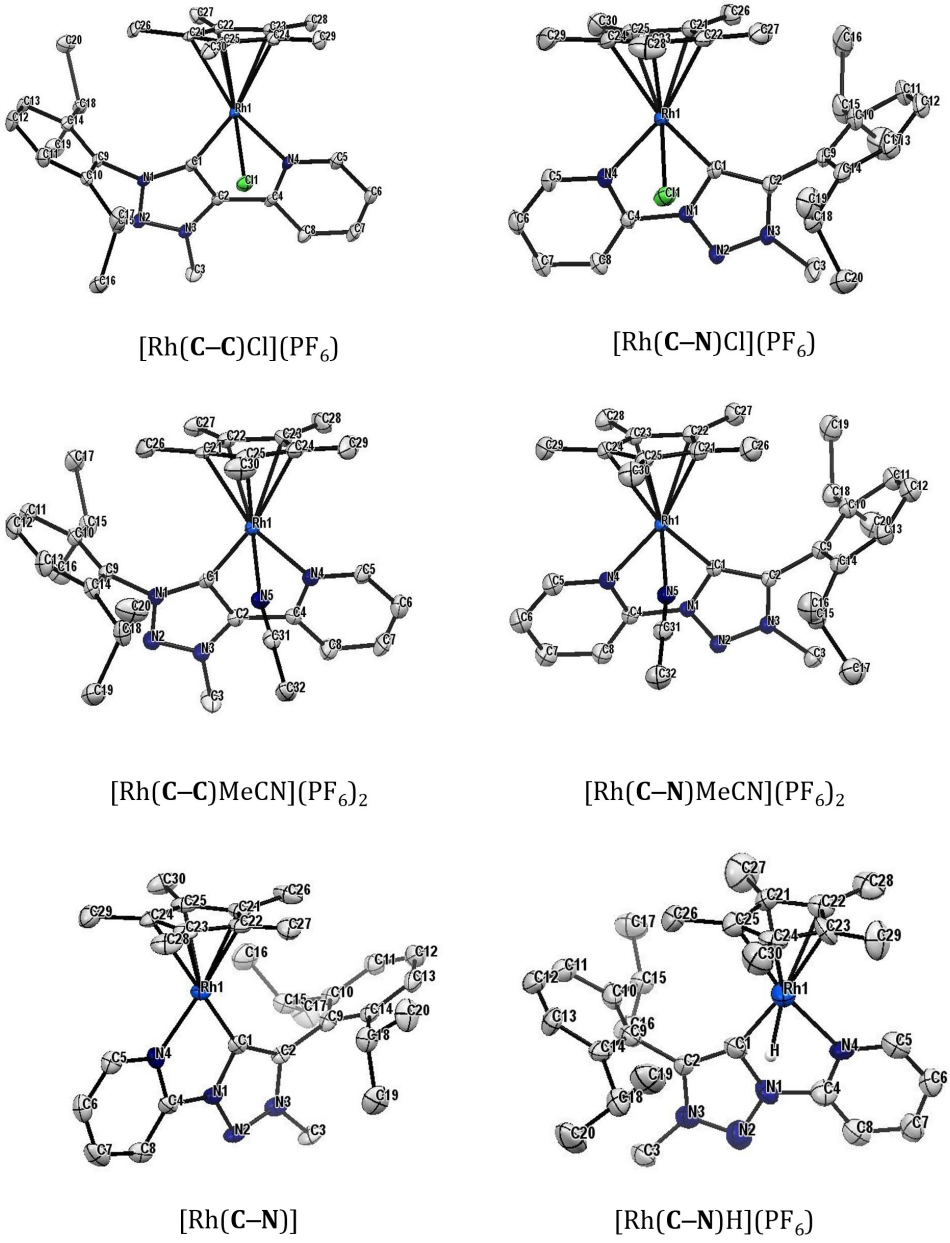

Figure 1. ORTEP representation of top left: [Rh(**C**–**C**)Cl](PF$_6$), top right: [Rh(**C**–**N**)Cl](PF$_6$), center left: [Rh(**C**–**C**)MeCN](PF$_6$)$_2$, center left: [Rh(**C**–**N**)MeCN](PF$_6$)$_2$, center right: [Rh(**C**–**N**)MeCN](PF$_6$)$_2$, bottom left: [Rh(**C**–**N**)] and bottom right: [Rh(**C**–**N**)H](PF$_6$) (carbon-hydrogens and counter ions are omitted for clarity). Ellipsoids are drawn with 50% probability.

crystalline material (40%) obtained for [Rh(**C**–**C**)H](PF$_6$) was not suitable for X-ray diffraction analysis.

The $^{13}C\{^1H\}$ NMR spectra of the presented complexes show characteristic doublet signals in the range of 170–160 MHz with Rh-MIC coupling constants between $J_{Rh,MIC}$ = 53–48 Hz.[24,33]

In the molecular structures in the crystal, the rhodium center in the complexes [Rh(**C**–**C**)Cl](PF$_6$), [Rh(**C**–**N**)Cl](PF$_6$), [Rh(**C**–**C**)MeCN](PF$_6$)$_2$ and [Rh(**C**–**N**)MeCN](PF$_6$)$_2$ display a three-legged piano-stool type geometry (Figure 1). The complexes show a η^5 mode from the Cp* ligand to the rhodium center with a metal-carbon bond length between 2.136(4)–2.227(1) Å. The angles between the planes of the Cp* ligand and the plane of the pyridyl-MIC coordination pocket at the rhodium center ((C1-N1-C4-N4) for [Rh(**C**–**N**)Cl](PF$_6$) and [Rh(**C**–**N**)MeCN](PF$_6$)$_2$ or (C1-C2-C4-N4) for [Rh(**C**–**C**)Cl](PF$_6$) and [Rh(**C**–**C**)MeCN](PF$_6$)$_2$, respectively) are in the range between 49.1°–56.7°, similar to those of [RhCp*(bpy)Cl]$^+$.[34] The complexes show a η^5 mode from the Cp* ligand to the rhodium center with a metal-carbon bond length between 2.136(4)–2.227(1) Å. The angles between the planes of the Cp* ligand and the plane of the pyridyl-MIC coordination pocket at the rhodium center ((C1-N1-C4-N4) for [Rh(**C**–**N**)Cl](PF$_6$) and [Rh(**C**–**N**)MeCN](PF$_6$)$_2$ or (C1-C2-C4-N4) for [Rh(**C**–**C**)Cl](PF$_6$) and [Rh(**C**–**C**)MeCN](PF$_6$)$_2$, respectively) are in the range between 49.1°–56.7°, similar to those of [RhCp*-(bpy)Cl]$^+$.[34] In contrast, an almost orthogonal geometry of the Cp* plane and the plane within the pyridyl-MIC coordination

pocket (C1-N1-C4-N4) are observed in [Rh(**C**–**N**)H](PF_6) and [Rh(**C**–**N**)] (Figure 1).

In the case of the hydrido complex [Rh(**C**–**N**)H](PF_6), the angle between the two planes is 83.5°, whereas the [Rh(**C**–**N**)] complex displays an angle of 86.0°. The drastic change in the geometry around the rhodium center results in the elongation of the Rh-Cp* bond distance between 0.025 Å and 0.051 Å (Table 1, see SI, **3**).

The comparison of the piano-stool complexes with the almost orthogonal oriented complexes indicates a significant delocalization from the rhodium center to the pyridyl-MIC ligand in [Rh(**C**–**N**)] and [Rh(**C**–**N**)H](PF_6). The increased π−backbonding results in a decrease of the metal-pyridyl-*N* and metal-MIC bond distances. The Rh-N bond lengths decreases from 2.120(3)–2.140(3) Å to 2.122(9) Å for [Rh(**C**–**N**)H](PF_6) and 2.006(5) Å for [Rh(**C**–**N**)], while the Rh–C(MIC) bond distances shorten from 2.051(1)–2.063(3) Å to 2.015(1) Å and 1.960(6) Å, respectively. Additionally, the formally reduced [Rh(**C**–**N**)] complex reveals an increase in the electron-density in the chelating C1-N1-C4-N4 framework (Table 1), indicated by the changes from partially C–N double bond character (∼1.37 Å) to an increased C–N single-bond character (∼1.40 Å) and *vice versa*. Only minimal changes in the intra-ligand (pyridyl-MIC) bond distances are observed other than those directly involved in the chelating pocket (see SI, Table S2 and S3). These data are thus an indication of a predominantly rhodium-based reduction, changing the formally Rh^{+III} center to a formally Rh^{+I} center.

Table 1. Selected bond lengths of [Rh(C–C)Cl](PF_6), [Rh(C–C)MeCN](PF_6)$_2$, [Rh(C–N)Cl](PF_6), [Rh(C–N)MeCN](PF_6)$_2$, [Rh(C–N)H](PF_6) and [Rh(C–N)].

	Bond lengths / Å	
Atoms	[Rh(C–C)Cl](PF_6)	[Rh(C–C)MeCN](PF_6)$_2$
Rh1-C1	2.052(3)	2.057(4)
C1-C2	1.388(4)	1.388(5)
C2-C4	1.454(4)	1.451(5)
C4-N4	1.357(4)	1.362(4)
N4-Rh1	2.120(3)	2.137(3)
Rh1-C21	2.175(3)	2.158(3)
Rh1-C22	2.150(3)	2.136(4)
Rh1-C23	2.173(3)	2.177(4)
Rh1-C24	2.201(3)	2.199(4)
Rh1-C25	2.191(3)	2.198(4)
	[Rh(C–N)Cl](PF_6)	[Rh(C–N)MeCN](PF_6)$_2$
Rh1-C1	2.051(1)	2.063(3)
C1-N1	1.370(2)	1.373(4)
N1-C4	1.405(1)	1.407(5)
C4-N4	1.332(2)	1.327(5)
N4-Rh1	2.133(2)	2.140(3)
Rh1-C21	2.143(1)	2.139(4)
Rh1-C22	2.143(1)	2.155(4)
Rh1-C23	2.227(1)	2.156(4)
Rh1-C24	2.213(1)	2.221(4)
Rh1-C25	2.138(1)	2.205(4)
	[Rh(C–N)H](PF_6)	[Rh(C–N)]
Rh1-C1	2.015(1)	1.960(6)
C1-N1	1.403(1)	1.394(7)
N1-C4	1.423(1)	1.374(7)
C4-N4	1.342(1)	1.369(7)
N4-Rh1	2.122(9)	2.006(5)
Rh1-C21	2.260(1)	2.192(6)
Rh1-C22	2.244(1)	2.245(6)
Rh1-C23	2.203(2)	2.241(5)
Rh1-C24	2.175(2)	2.241(6)
Rh1-C25	2.158(2)	2.245(6)

Hydride Reactivity

Transition-metal hydride complexes play a key role in the electrocatalytic H_2 formation.[2,3,9–11,35,36] The reactive intermediates can act as transferring reagent for H^+, $H^{\cdot}$ or H^- and are of particular interest in the design of the electrocatalyst. However, the investigation of the hydride species remains challenging due to the high reactivity and instability in coordinating solvents. Hence, the isolation of the diamagnetic [Rh(**C**–**C**)H](PF_6) and [Rh(**C**–**N**)H](PF_6) allows us to shine light on the reactivity of the metal bound hydride species (Scheme 3, see SI **7**).

In the ^{1}H NMR spectrum, both the hydride complexes show a metal-bound hydride signal at −11.46 ppm ($J_{Rh,H}$ = 22.0 Hz) and −11.48 ppm ($J_{Rh,H}$ = 23.1 Hz), respectively, similar to the hydride shift reported for electron-rich diphosphine ligands (see SI, **2.50** and **2.60**).[19] There is no evidence for the H^+ migration into the Cp* ligand, (even under variable temperature conditions) which would result in three inequivalent methyl resonances (see SI, Figure S10).[15,16] The strong σ−donating properties of the MIC-moieties lead to an increased electron density at formally Rh^{+III} centers, favoring the formation of the metal-bound [HRhCp*] complexes instead of the protonated [RhCp*H] complexes.

Further investigations by IR spectroscopy clearly confirm the metal-bound hydride species with a Rh-H stretching at $\tilde{\nu}$(Rh-H) = 1956 cm^{-1} for [Rh(**C**–**C**)H](PF_6) and at 1953 cm^{-1} for [Rh(**C**–**N**)H](PF_6) (see SI, Figure S12 and S15). The Rh–H stretching frequencies are located between the earlier reported bpy and diphosphine based [Rh(Cp*)] hydride analogues, elucidating the synergy between reactivity and stability.[19,37]

The addition of $NaBH_4$ to the Rh-hydrides results in the formation of [Rh(**C**–**N**)] and [Rh(**C**–**C**)] (see SI, **7.10**) under evolution of H_2. The ^{1}H NMR shows a strong high field shift of the aromatic signals up to 6.53 ppm, confirming the strongly reduced character of the pyridyl-MIC ligands and the H^+ reactivity in [Rh(**C**–**N**)] and [Rh(**C**–**C**)].

Treatment of [Rh(**C**–**C**)H](PF_6) and [Rh(**C**–**N**)H](PF_6) with TEMPO (=(2,2,6,6-tetramethylpiperidin-1-yl)oxyl)) at room temperature results in a rapid formation of a EPR-active 17 VE species (Figure 2, see SI, **7.20**).

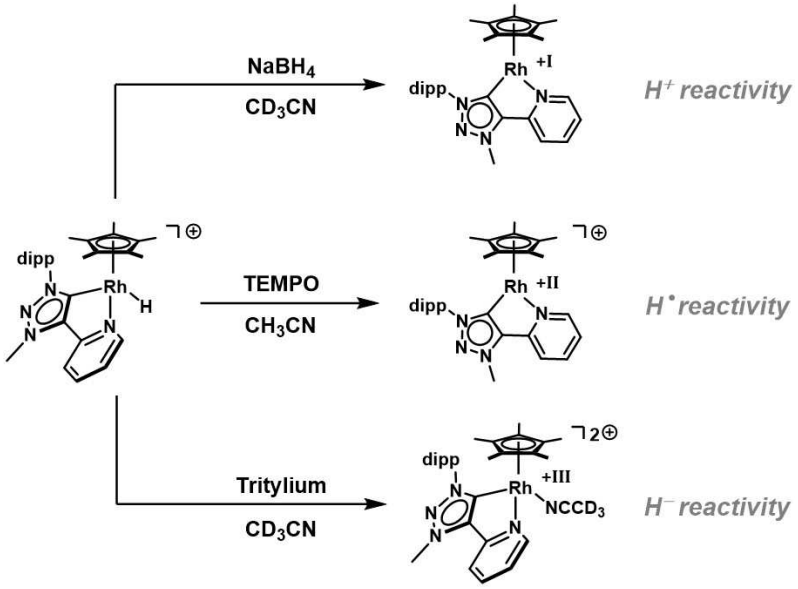

Scheme 3. Reactivity of [Rh(**C**–**C**)H](PF$_6$) as a H$^+$, H$^\cdot$ or H$^-$ in CD$_3$CN at room temperature. The same reaction conditions were applied for [Rh(**C**–**N**)H](PF$_6$) (see experimental section).

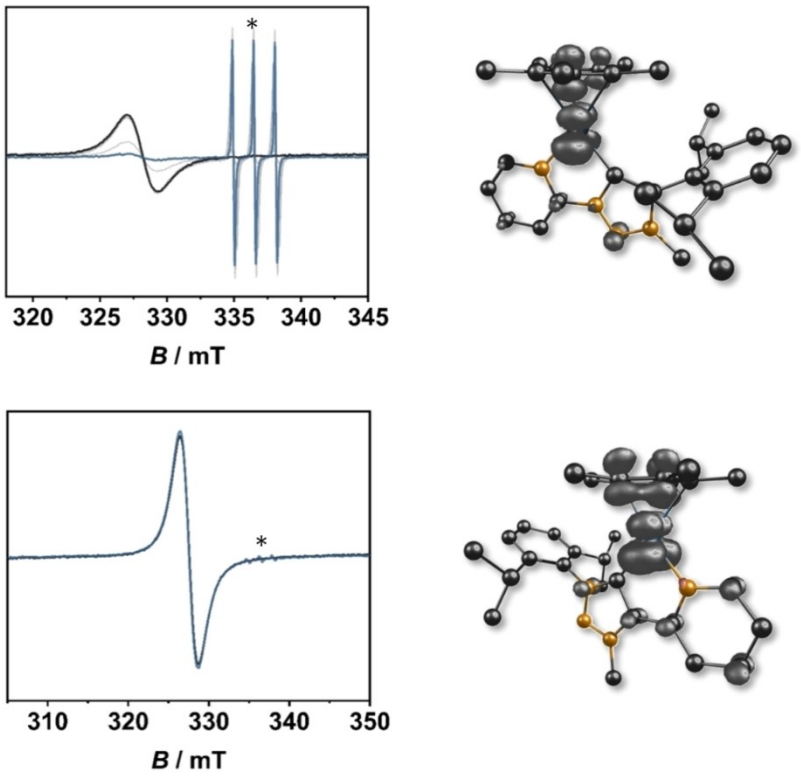

Figure 2. EPR spectra of [Rh(**C**–**N**)]$^+$ (top left) and [Rh(**C**–**C**)]$^+$ (bottom left) generated after addition of TEMPO to a CH$_3$CN solution of [Rh(**C**–**N**)H](PF$_6$) or [Rh(**C**–**C**)H](PF$_6$), respectively, over a 10 minute period (* = unreacted TEMPO) at room temperature (g = 2.06) and spin density plot of [Rh(**C**–**N**)]$^+$ (top right) and [Rh(**C**–**C**)]$^+$ (bottom right) (Rh = 46% for both complexes) with PBE0/RIJCOSX/D3BJ/def2-TZVP (iso value = 0.006).

The isotropic signal at a g-value of 2.06 for both complexes at room temperature is characteristic for a Rh(II) species.[36,38] Upon cooling, the EPR signal diminishes, most likely as consequence of dimerization of two EPR-active species. The EPR signal can be recovered by allowing the sample to warm up to room temperature again, further supporting the dimerization of the EPR-active intermediate. The isolation of the respective Rh(II) species failed due to the lack of stability during the crystallization attempts in the glovebox, indicated by a color

change from a purple-grey to a colorless solution with a colorless precipitate.

In the case of $[Rh(\mathbf{C}–\mathbf{C})]^+$ a rhombic signal could be detected at low temperatures with $g_1 = 2.16$, $g_2 = 2.05$ and $g_3 = 1.98$ at −100 °C. The high g−anisotropy of $\Delta g = 0.11$ supports the strong metal contribution of the radical species (see SI, **7.20**), which is also reflected in the spin density plot of the coordinatively unsaturated $[Rh(\mathbf{C}–\mathbf{C})]^+$ (Rh = 46 %) compared to the coordinatively saturated solvent adduct $[Rh(\mathbf{C}–\mathbf{C})MeCN]^+$(Rh = 1 %). The above results indicate that the dimerization of the formally Rh^{II} based species is slower for $[Rh(\mathbf{C}–\mathbf{C})]^+$ in comparison to $[Rh(\mathbf{C}–\mathbf{N})]^+$.

The amphiphilic reactivity of $[Rh(\mathbf{C}–\mathbf{C})H](PF_6)$ and $[Rh(\mathbf{C}–\mathbf{N})H](PF_6)$ motivated us to further investigate the hydride transfer reactivity with $Ph_3C(PF_6)$ (= tritylium) in CD_3CN at room temperature (see SI, **7.30**). In the case of $[Rh(\mathbf{C}–\mathbf{N})H](PF_6)$, a clean conversion to triphenylmethane ($Ph_3C–\underline{H}$ = 5.61 ppm) under the formation of $[Rh(\mathbf{C}–\mathbf{N})MeCN\text{-}d_3](PF_6)_2$ was observed, while the reaction of $[Rh(\mathbf{C}–\mathbf{C})H](PF_6)_2$ with $Ph_3C(PF_6)$ leads to a mixture of $[Rh(\mathbf{C}–\mathbf{C})(MeCN\text{-}d_3)](PF_6)_2$, triphenylmethane, the starting material and an unknown species without any detectable metal-hydride signal in the ^{1}H NMR spectrum. Thus, the Rh-hydride complexes present here can act as either H^+, $H^\cdot$ or H^- transfer reagents displaying their true ambivalent nature.

The estimation of the pK_a values, bond dissociation free energies (BDFE) and hydricities ($\Delta G^0_{H^-}$) was performed according to the correlation reported by Waldie *et al.* on the basis of the reduction potentials of the parent complexes in $[Rh(\mathbf{C}–\mathbf{C})MeCN](PF_6)$ and $[Rh(\mathbf{C}–\mathbf{C})MeCN](PF_6)$ (see cyclic voltammetry).[39]

The comparatively low pK_a values of 22.0 kcal/mol for $[Rh(\mathbf{C}–\mathbf{C})H]^+$ and 20.3 kcal/mol in the case of $[Rh(\mathbf{C}–\mathbf{N})H]^+$ emphasize a strong stabilization of the respective Rh(I) species by the excellent σ−donor and π−acceptor properties pyridyl-MIC ligands. The higher π−acceptor capacity of the C–N linked pyridyl-MIC ligand compared to its C–C linked counterpart likely results in an advantageous distribution of the electron density between the orthogonal oriented C–N ligand and the electron donating Cp* moiety in $[Rh(\mathbf{C}–\mathbf{N})]$.[40] In contrast, the analogues cyclometallated pyridyl-phenyl [RhCp*] hydride complexes reported by Norton *et al.* show pK_a values of 30.3 kcal/mol in acetonitrile.[36] The anionic nature of the cyclometallated ligand probably results in a destabilization of the Rh(I) species compared to the neutral pyridyl-MIC ligand.

The greater σ−donor properties of the C–C linked pyridyl-MIC ligand compared to the C–N linked constitutional isomer lead to a slightly lower BDFE in in $[Rh(\mathbf{C}–\mathbf{C})H]^+$ with 49.6 kcal/mol and 50.0 kcal/mol in $[Rh(\mathbf{C}–\mathbf{N})H]^+$ indicating an increased stabilization of the respective Rh(II) species.

However, these results should be taken with care as an identical hydricity of $\Delta G^0_{H^-} = 56.2$ kcal/mol is assigned for both complexes following the correlation by Waldie *et al.*. Future studies in our laboratories will focus on the direct determination of the experimental pK_a values, BDFE and $\Delta G^0_{H^-}$.

Cyclic Voltammetry

The electrochemical activation of polypyridine [RhCp*] complexes has been intensively studied over the past decades.[2,3,9–13,15,16,18] A 2e$^-$ reduction of Rh^{III} to Rh^{I} and the corresponding re-oxidation back to the Rh^{III} species is usually observed in these systems.

In contrast to previous reports on polypyridine [RhCp*] complexes, the 2e$^-$ reduction of $[Rh(\mathbf{C}–\mathbf{C})Cl](PF_6)$ and $[Rh(\mathbf{C}–\mathbf{N})Cl](PF_6)$ at $E^{red}_{p,c} = -1.46$ V and $E^{red}_{p,c} = -1.34$ V generates two new species in the re-oxidation cycle along with a shift of the anodic potential at $E^{ox1'}_{p,a} = -1.19$ V and $E^{ox2'}_{p,a} = -1.05$ V for $[Rh(\mathbf{C}–\mathbf{C})Cl](PF_6)$, and $E^{ox2'}_{p,a} = -1.12$ V and $E^{ox2'}_{p,a} = -1.03$ V for $[Rh(\mathbf{C}–\mathbf{N})Cl](PF_6)$, respectively (Figure 3).

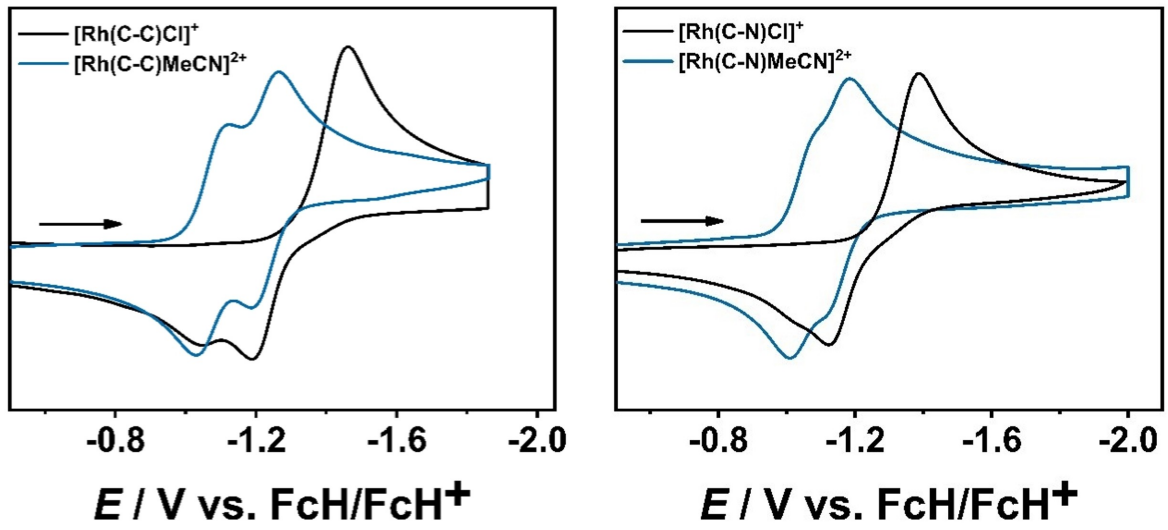

Figure 3. Comparison of the cyclic voltammograms of $[Rh(\mathbf{C}–\mathbf{C})Cl](PF_6)$ and $[Rh(\mathbf{C}–\mathbf{C})MeCN](PF_6)_2$ (left) and $[Rh(\mathbf{C}–\mathbf{N})Cl](PF_6)$ and $[Rh(\mathbf{C}–\mathbf{N})MeCN](PF_6)_2$ (right) in CH_3CN and 0.1 M Bu_4NPF_6 with a scan rate of 100 mV/s.

The first 2e⁻ reduction is shifted according to the overall π−acceptor capacities of the two ligands, described earlier by our group.[27,40] The C–C linked ligand displays a weaker π−acceptor ability, compared to its C–N linked counterpart. After 2e⁻ reduction, subsequent chloride dissociation takes place, leading to the formation of the respective [Rh(**C**–**C**)] and [Rh(**C**–**N**)] complexes. The drastic structural reorganization initiates an electronic re-distribution from the predominantly pyridyl-MIC centered electron to the central metal atom, formally generating a Rh^{+I} metal center.

Reversing the scan direction shows two distinct one-electron oxidations. According to our assumption, the first oxidation can be assigned to a Rh(I)/Rh(II) redox couple. The Rh(I)/Rh(II) redox couple of the respective complexes is shifted according to the overall σ−donor strength of the respective ligands.[40] The higher overall σ−donor properties of the C–C linked ligand leads to a greater destabilization of the rhodium-centered orbitals, as indicated by the cathodic shift at $E_{1/2}^{ox1'} = -1.18$ V. In contrast, the weaker σ−donor strength of the C–N linked counterpart results in an anodic shift of the metal-centered oxidation at $E_{1/2}^{ox1'} = -1.11$ V.

The second oxidation at $E_{p,a}^{ox2'} = -1.03$ V, for the C–C linked complex, and at $E_{p,a}^{ox2'} = -1.01$ V, for the C–N linked counterpart, display nearly identical oxidation potentials. Therefore, the second oxidation can be assigned to the Rh(II)/Rh(III) redox couple, resulting in the respective solvato complexes.

With the acetonitrile adducts in hand, we examined the electrochemical transformation in cyclic voltammetry (Figure 3, see SI, **4.30**). Both complexes show two separated one-electron reduction processes. The high peak-to-peak separation ($\Delta E_{p,c}^{red1}$ =90 mV) of the first reduction at $E_{p,c}^{red1} = -1.06$ V, for both complexes, provides first indications of a structural reorganization accompanied by the loss of the acetonitrile ligand after the first metal-centered reduction (for details, see **4**. and **5.**).

In contrast, the second reduction at $E_{1/2}^{red2} = -1.24$ V, for [Rh(**C**–**C**)MeCN](PF$_6$)$_2$, and $E_{1/2}^{red2} = -1.15$ V, for [Rh(**C**–**C**)MeCN](PF$_6$)$_2$, display a smaller peak-to-peak separation of $\Delta E_{1/2}^{red2}$ =70 mV for both complexes. The second reduction potential follows the same trend in the π−acceptor properties of the ligands, as earlier described for the respective chlorido [RhCp*] complexes. The decreased peak-to-peak separation indicates a minor structural reorganization and further supports the partially loss of the acetonitrile ligand.

Furthermore, complex [Rh(**C**–**N**)] was investigated by cyclic voltammetry (Figure 4). Starting from an initial potential of −1.73 V, the Rh(I)/Rh(II) and Rh(II)/Rh(III) redox couple are in good agreement with the reduction processes observed for [Rh(**C**–**N**)MeCN](PF$_6$)$_2$. This match also further confirms the dissociation of the solvent molecule upon one electron reduction of the acetonitrile complexes as discussed above.

All complexes show a further third irreversible reduction at $E_{p,c}^{red3} = -2.69$ V for [Rh(**C**–**C**)] and $E_{p,c}^{red3} = -2.81$ V for [Rh(**C**–**N**)], respectively.

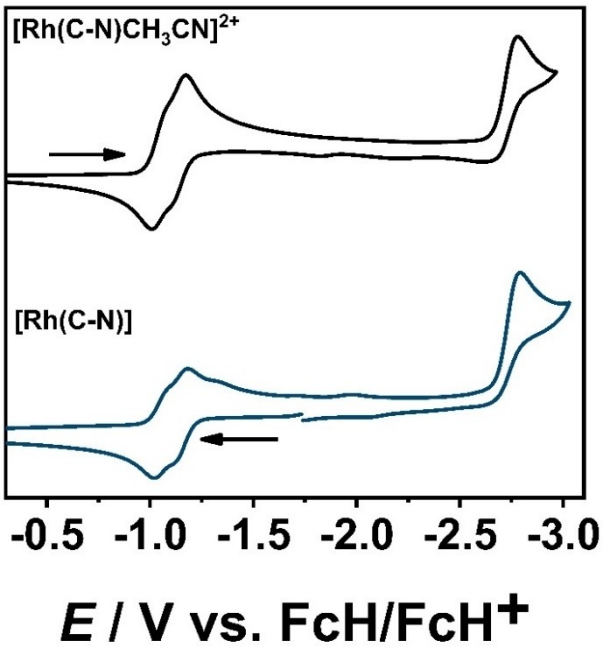

Figure 4. Comparison of [Rh(**C**–**N**)MeCN](PF$_6$)$_2$ (top, black) and [Rh(**C**–**N**)] (bottom, blue) in CH_3CN and with 0.1 M Bu_4NPF_6 with a scan rate of 100 mV/s.

Electrochemical H^+ Reduction

To investigate the precatalytic activation in the electrochemical H^+ reduction, all complexes were tested in presence acetic acid (=AcOH) as proton source (Figure 5, see SI, **8**). The two-electron reduced forms of the solvent complexes [Rh(**C**–**C**)MeCN](PF$_6$)$_2$ and [Rh(**C**–**N**)MeCN](PF$_6$)$_2$ are excellent candidates to provide useful insights in the precatalytic activation to generate the corresponding [RhCp*] hydride complexes.

In the presence of acetic acid, the first reduction, which results in the loss of acetonitrile remains intact (Figure 5). However, addition of one equivalent of the acid shifts the second reduction to more anodic potential, indicating the formation of new species at −1.21 V for [Rh(**C**–**C**)MeCN](PF$_6$)$_2$ and −1.14 V for [Rh(**C**–**N**)MeCN](PF$_6$)$_2$, which undergo an additional reduction at −2.11 V and −1.97 V, respectively.

However, the addition of more equivalents shifts the potential only slightly to more anodic potential (−1.18 V for [Rh(**C**–**C**)MeCN](PF$_6$)$_2$ and −1.11 V for [Rh(**C**–**N**)MeCN](PF$_6$)$_2$) without significantly influencing the current. In contrast, the current at −1.97 V constantly increases, indicating the catalytic conversion of H^+ in presence of the catalysts.

The stepwise addition of five equivalents shows an interesting trend: one-electron reduction of Rh^{III} to Rh^{II} turns into a two-electron reduction, as indicated by the increased current, while the Rh^{II}/Rh^{I} redox couple is no longer apparent. This observations emphasize a rapid CE mechanism or a proton-coupled electron transfer (PCET) after the first reduction and subsequent loss of acetonitrile.[41] We have performed tentative calculations of TOF for these catalysts at low proton concentrations (see section 8, SI). However, as the catalytic current with these

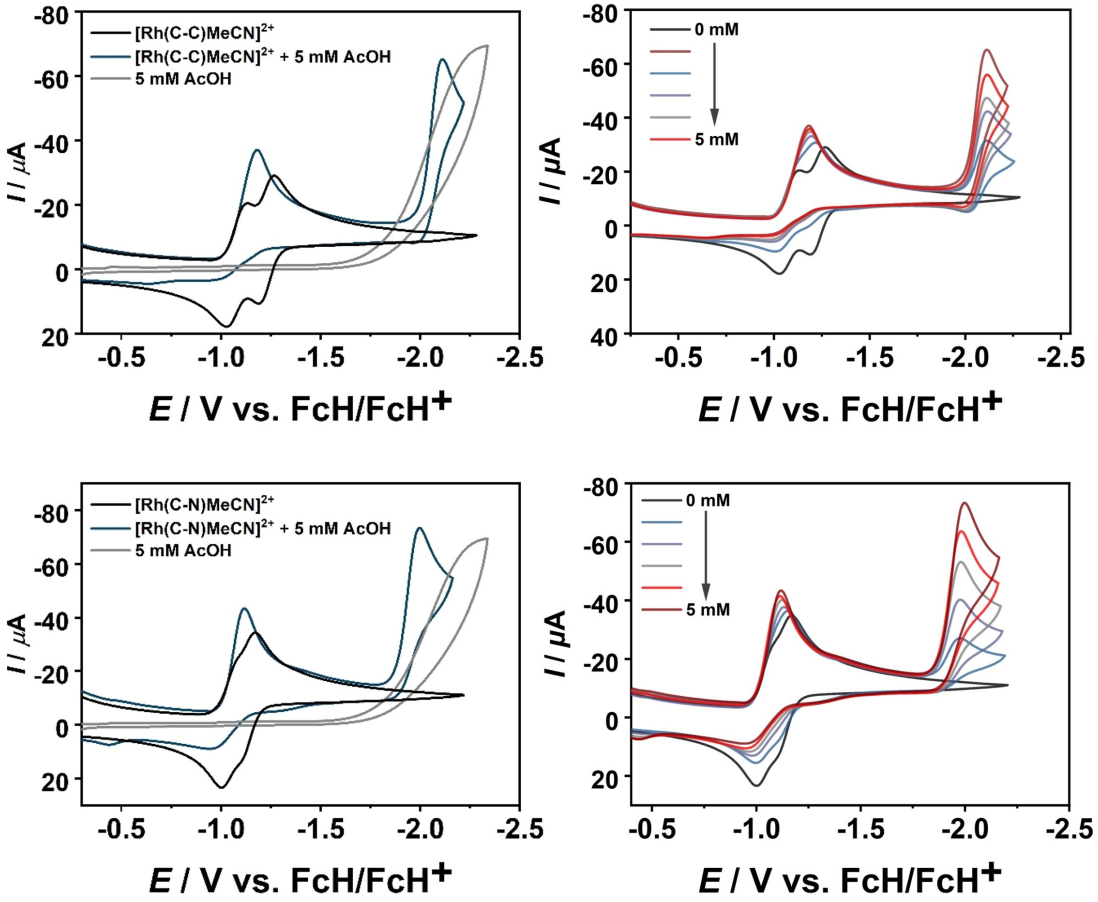

Figure 5. Electrochemical H^+ reduction with [Rh(**C**–**C**)MeCN]$(PF_6)_2$ (top) and [Rh(**C**–**N**)MeCN]$(PF_6)_2$ (bottom) (1 mM) in CH_3CN and 0.1 M Bu_4NPF_6 with a scan rate of 100 mV/s (left: black = without AcOH, grey = only AcOH, green = with 10 mM AcOH) and at low concentrations of AcOH (right).

complexes are almost in the region of the background current of the direct reduction of the protons at the electrode surfaces (see control measurements, section 8, SI), these values should be taken with caution.

Taking all the data together, the first reduction results in the dissociation of the acetonitrile ligand, generating the coordinatively unsaturated Rh(II) complexes, which can undergo a either a CE mechanism or a PCET to form the respective [RhCp*]-hydride complexes.

An additional electron-transfer is required to initiate the electrocatalytic H^+ reduction. Unfortunately, the [RhCp*]-hydride complexes are not sufficiently stable under the electrochemical conditions, indicated by a drastically color changes after couple of minutes, even under fully inert conditions (see SI, **4.50** and **4.60**). Therefore, we turned our focus to UV/vis/NIR (spectro−)electrochemistry (UV/vis/NIR-SEC).

UV/vis/NIR (Spectro−)electrochemistry

UV/vis/NIR SEC is a powerful technique to detect short-lived intermediates in electron-transfer processes. In combination with (TD)-DFT calculations, detailed mechanistic insights can be provided to understand the precatalytic formation.[4,12,28,29]

The well-separated multi-electron processes makes [Rh(**C**–**C**)MeCN]$(PF_6)_2$ a good candidate to study in UV/vis/NIR-SEC. The complex displays a featureless UV/vis spectrum with several mixed metal-ligand-to-ligand charged transfer (MLLCT) and ligand-to-metal-charge transfer (LMCT) bands, indicated by the bright yellow color of the complex (see SI, **6.40**), while the chloride containing complex features an additional metal-chloride-to-ligand charge transfer band (MXLCT).

Upon reduction to [Rh(**C**–**C**)], the UV/vis/NIR spectrum shows intense absorption bands in the visible and near-infrared range around 823 nm, 589 nm and 436 nm, which can be assigned to different MLCT bands from the rhodium center with small contribution of the Cp* ligand to the pyridyl-MIC ligand (Figure 6, see SI, **6.80**). The two-electron reduction is accordingly accompanied by a color change from light yellow to dark green. The same trend in this regard is observed in the case of complex [Rh(**C**–**N**)MeCN]$(PF_6)_2$. Upon reduction, [Rh(**C**–**N**)] turns dark purple in color and a blue-shift of the MLCT bands is observed. The chloride containing complexes display identical absorption spectra after two-electron reduction as the ones described above and are in good agreement with the previously described electrochemical data.

During the reduction of [Rh(**C**–**C**)MeCN]$(PF_6)_2$ in SEC experiments, an intermediate could be detected. Our TD-DFT

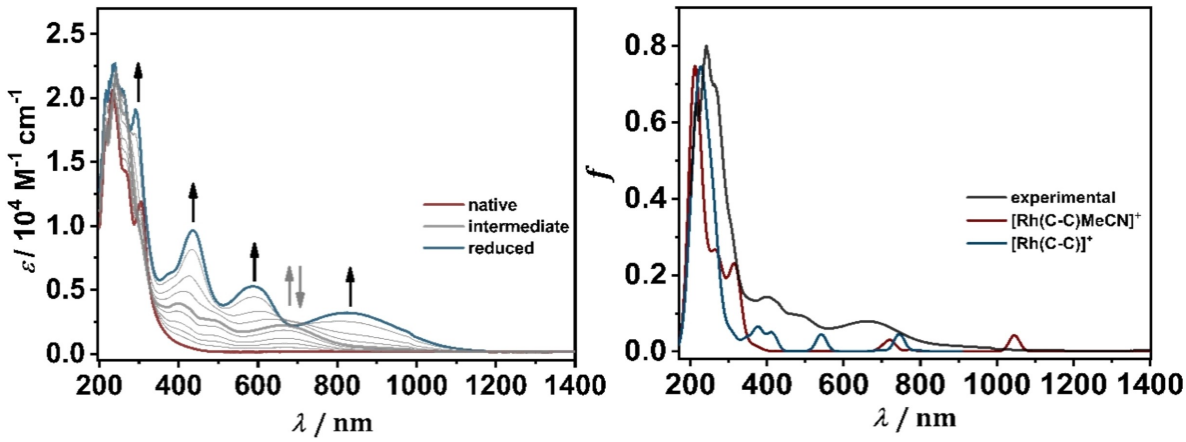

Figure 6. Changes in the UV/vis/NIR spectra of [Rh(**C**–**C**)MeCN]$(PF_6)_2$ in CH_3CN/0.1 M Bu_4NPF_6 during the first two reductions with a Au working electrode (left) and calculated spectra (right, PBE0/RIJCOSX/D3BJ/def2-TZVP, FWHM = 32) of [Rh(**C**–**C**)MeCN]$^+$ (red), [Rh(**C**–**C**)]$^+$ (blue) in comparison with experimental intermediate (black, normalized).

calculations confirm the formation of the coordinatively unsaturated [Rh(**C**–**C**)]$^+$ complex (Figure 6, right: blue), instead of the solvent coordinated [Rh(**C**–**C**)MeCN]$^+$ complex (Figure 6, right: red), as indicated by the characteristic absorption bands between 380–600 nm. This is in good agreement with the aforementioned EPR spectra of [Rh(**C**–**C**)]$^+$ and [Rh(**C**–**N**)]$^+$ (Figure 2). The absorption bands observed for [Rh(**C**–**C**)]$^+$ display similar features as described for [Rh(**C**–**C**)]. The blue-shift is a consequence of the change in the formal oxidation state of the rhodium center from Rh(I) to Rh(II). To compensate the electron deficiency at the rhodium center, the Cp* ligand contributes stronger to the electronic transitions (see SI, **6.40** and **6.80**). The comparison of the spectra before and after bulk electrolysis reveals that even after the chemical transformation due to ligand dissociation, the initial spectra could be restored after SEC for all studied complexes. In the case of the chloride containing [RhCp*] complexes, it is reasonable to predict the formation of [Rh(**C**–**C**)MeCN]$(PF_6)_2$ and [Rh(**C**–**N**)MeCN]$(PF_6)_2$ after SEC due to chloride dissociation and solvent coordination.

However, according to our spectroelectrochemical data, the coordination of the chloride takes place when sweeping back to the anodic potential (see SI, **5.10** and **5.20**). This observation could have a drastic impact on electrocatalysis, as the chloride, in the vicinity of the reduced [RhCp*] complex, can influence the preequilibrium during electrochemical H^+ reduction.

No intermediates in the visible spectrum could be detected during the reduction process in the presence of acetic acid, likely confirming a rapid CE mechanism or PCET in the electrochemical generation of [Rh(**C**–**C**)H](PF_6) and [Rh(**C**–**N**)H](PF_6) (Figure 7). The absorption spectra show a characteristic metal-hydride-to-ligand charge transfer (MHLCT) at 430 nm and 444 nm, respectively, which are in good agreement with our TD-DFT calculations (PBE0/RIJCOSX/D3BJ/def2-TZVP, see SI, **6.6** and **6.7**).

With the [RhCp*] hydride complexes and the reduced complexes in hand, we compared the electrochemically generated species with the chemically isolated complexes (Figure 8, see SI, **5.50**).

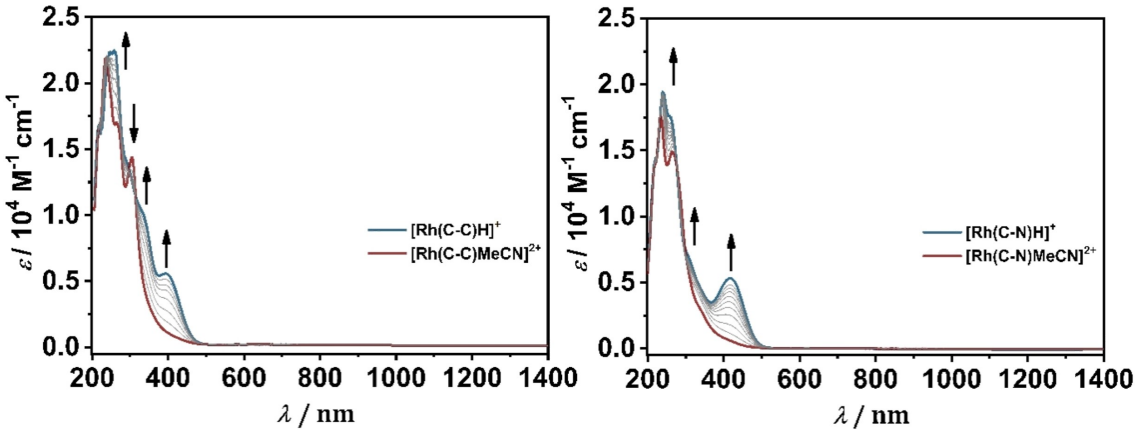

Figure 7. Changes in the UV/vis/NIR spectra of [Rh(**C**–**C**)MeCN]$(PF_6)_2$ (left) and [Rh(**C**–**N**)MeCN]$(PF_6)_2$ (right) in CH_3CN/0.1 M Bu_4NPF_6 during the two reductions in presence of excess AcOH with a Au working electrode.

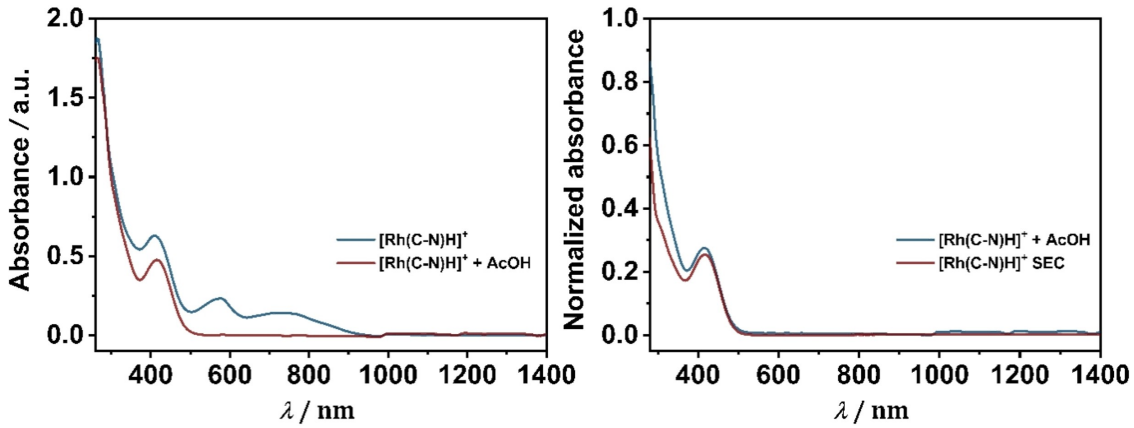

Figure 8. Left: UV/vis/NIR spectra of [Rh(**C**–**N**)H](PF$_6$) (blue) and after addition of an excess AcOH in CH$_3$CN (red). Right: Comparison of the UV/vis/NIR spectra of the chemically isolated [Rh(**C**–**N**)H](PF$_6$) (blue) and after bulk electrolysis with an Au working electrode in presence of an excess AcOH (red) in CH$_3$CN/0.1 M Bu$_4$NPF$_6$.

In the case of [Rh(**C**–**N**)], the absorption spectrum of the isolated complex shows the same transitions as observed for the electrochemically generated species, while the isolated [Rh(**C**–**N**)H](PF$_6$) complex shows a mixture of [Rh(**C**–**N**)] and [Rh(**C**–**N**)H](PF$_6$) generated during SEC. Addition of excess acetic acid exclusively generates the [RhCp*] hydride complex indicating an equilibrium between [Rh(**C**–**N**)] and the weakly bound hydride in [Rh(**C**–**N**)H](PF$_6$).

To our surprise, the electrochemically and chemically generated spectra of [Rh(**C**–**C**)] are not identical in acetonitrile. However, changing the solvent to THF results in a good fit of both spectra (see SI, **5.51**). A plausible explanation might be solvent effects causing degradation in presence of light.

In the case of [Rh(**C**–**C**)H](PF$_6$), the chemically isolated complex and the electrochemically generated species fit well, beside the presence of a second unknown species, which diminish upon addition of acetic acid. Unfortunately, our spectroscopic and electrochemcial data do not provide any convincing evidence to assign the nature of the unknown species due to the absence of additional hydride signals in the ^{1}H NMR.

Conclusions

In summary, we have presented the first isolation and a thorough characterization through crystallographic, spectroscopic and (spectro)electrochemical methods of solvato, hydrido, and reduced species of Cp*Rh complexes with pyridyl-mesoionic carbene ligands. A detailed mechanistic study of the precatalytic activation of pyridiyl-MIC [RhCp*] complexes is presented (Scheme 4). Cyclic voltammetric studies, combined with UV/vis/NIR-SEC measurements and theoretical calculations reveal a two-electron reduction process (Scheme 4, **E**^{1} and **E**^{2}) to generate the coordinatively unsaturated [RhCp*] complexes after ligand dissociation, which are the first of their kinds to be isolated and fully characterized.

In presence of acetic acid, a PCET is observed after the first reduction generating the [RhCp*] hydride complexes (Scheme 4, **E**$^{2'}$). The data presented here are of fundamental importance for the mechanistic understanding of a range of reductive electrocatalytic and homogeneous catalytic processes with metal complexes of pyridyl-MIC ligands. The utility of such complexes in several electrocatalytic processes, including a synthetic strategy to reduce their overpotential, and a detailed mechanistic understanding thereof are currently under investigation in our laboratories.

Experimental Section

General Procedures, Materials, and Instrumentation

Caution! Compounds containing azides are potentially explosive. Although we never experienced any problems during synthesis or analysis, all compounds should be synthesized only in small quantities and handled with great care! Unless otherwise noted, all reactions were carried out using standard Schlenk-line-techniques under an inert atmosphere of argon (Linde Argon 4.8, purity 99.998 %). Commercially available chemicals were used without further purification. The solvents used for metal complex synthesis and catalysis were available from MBRAUN MB-SPS-800 solvent System and degassed by standard techniques prior to use. The identity and purity of compounds were established via ^{1}H and ^{13}C NMR spectroscopy, elemental analysis and mass spectrometry. Solvents for cyclic voltammetry and UV/vis- and EPR-spectroelectrochemical measurements were dried and distilled under argon and degassed by common techniques prior to use. Column chromatography was performed over silica 60 M (0.04–0.063 mm). ^{1}H and ^{13}C{^{1}H} NMR spectra were recorded on a Bruker Avance 500 spectrometer at 19–22 °C. Chemical shifts are reported in ppm referenced to the residual solvent peaks.[42] The following abbreviations are used to represent the multiplicity of the signals: s (singlet), d (doublet), t (triplet), q (quartet), p (pentet), sept (septet), hept (heptet). Mass spectrometry was performed on an Agilent 6210 ESI-TOF. Elemental analyses were performed with an Elementar Micro Cube elemental analyser.

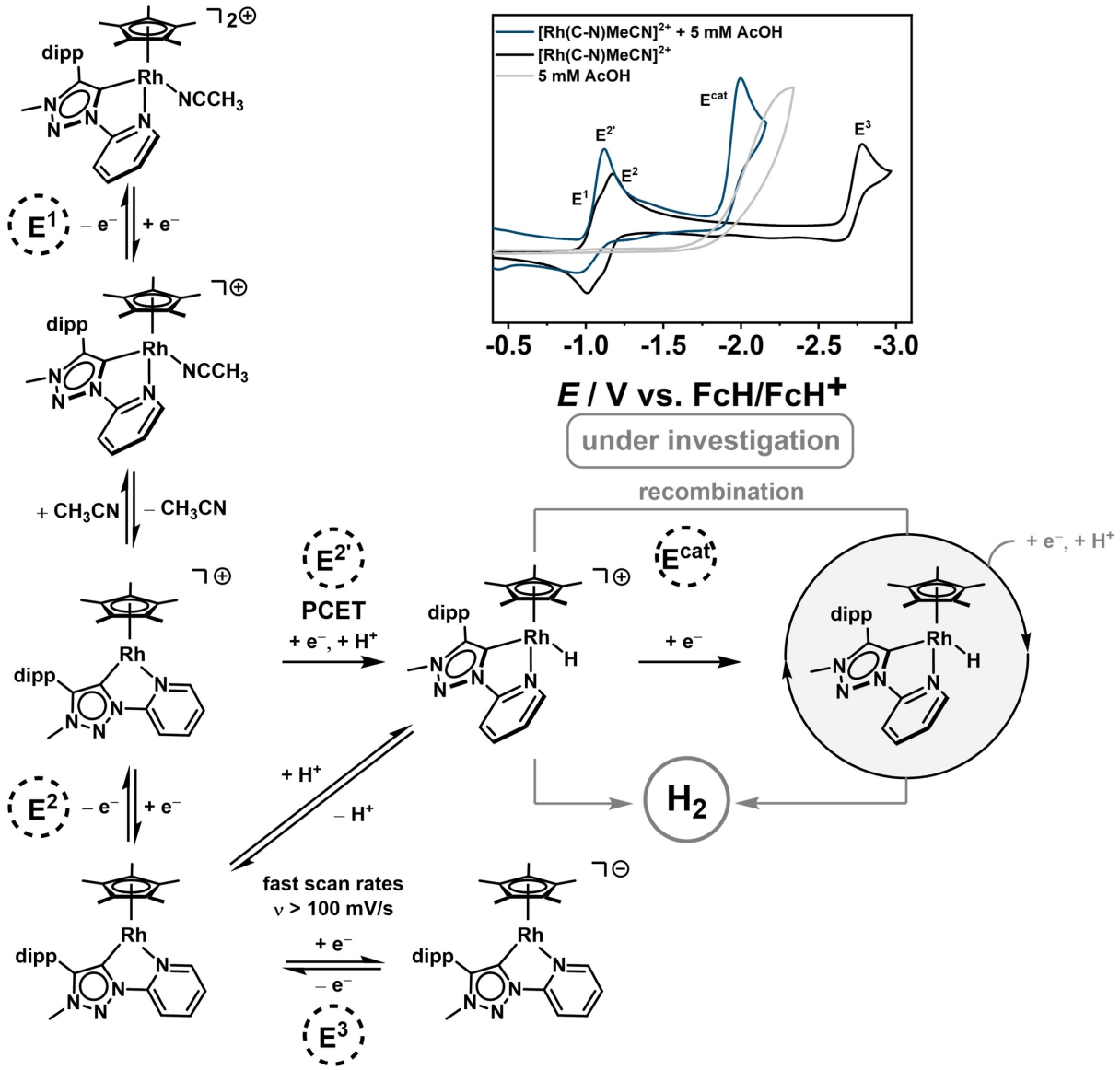

Scheme 4. Proposed precatalytic activation of [Rh(**C**–**N**)MeCN]$(PF_6)_2$ in CH_3CN/0.1 M Bu_4NPF_6 with a GC working electrode.

X-ray Diffraction

Deposition Numbers 2075636 (for [Rh(**C**–**C**)Cl](PF_6)), 2133478 (for [Rh(**C**–**C**)MeCN]$(PF_6)_2$), 2075640 (for [Rh(**C**–**N**)Cl](PF_6)), 2133502 (for [Rh(**C**–**N**)MeCN]$(PF_6)_2$), 2173197 (for [Rh(**C**–**N**)H](PF_6)), 2127781 (for [Rh(**C**–**N**)]) contain the supplementary crystallographic data for this paper. These data are provided free of charge by the joint Cambridge Crystallographic Data Centre and Fachinformationszentrum Karlsruhe Access Structures service. X-ray data were collected on a BRUKER Smart AXS, BRUKER D8 Venture or Bruker Kappa Apex2duo system. Data were collected at 100(2) or 140(2) K, respectively, using graphite-monochromatic Mo K_α radiation (λ_α =0.71073 Å). The strategy for the data collection was evaluated by using the APEX2 or Smart software. The data were collected by standard "ω scan techniques" or "$\omega - \varphi$ scan techniques" and were scaled and reduced using APEX2, SAINT+, and SADABS software. The structures were solved by direct methods using SHELXL-97 or intrinsic phasing using SHELXL-2014/7 and refined by full matrix least-squares with SHELXL-2014/7, refining on F^2. Non-hydrogen atoms were refined anisotropically. If it is noted, bond length and angles were measured with Mercury, version 3.8.[43]

Electrochemistry

Cyclic voltammograms were recorded with a PalmSens4 potentiostat with a conventional three-electrode configuration consisting of a glassy carbon working electrode, a platinum auxiliary electrode, and a coiled silver wire as a pseudo reference electrode. The (decamethyl)ferrocene/(decamethyl)ferrocenium couple was used as internal reference. All measurements were performed at room temperature with a scan rate between 25 and 1000 mVs^{-1}. The experiments were carried out in absolute acetonitrile containing 0.1 M Bu_4NPF_6 (Sigma Aldrich, ≥99.0%, electrochemical grade) as the supporting electrolyte. For electrocatalysis a solution of acetic acid (1 M) in acetonitrile was added to a 1 mM solution of the complex in steps of 5 μL or 25 μL and measured with all scan rates mentioned above. (Decamethyl)ferrocene/(decamethyl)ferrocenium couple (1 mg, 1 mM) was added as internal reference.

Spectroelectrochemistry

UV/vis spectra were recorded with a J&M TIDAS spectrometer and the IR spectra were performed with a Bruker FT-IR Spectrometer INVENIO. The spectroelectrochemical measurements were carried out in an optically transparent thin-layer electrochemical (OTTLE)[44] cell (CaF_2 windows) with a gold-mesh working electrode, a platinum-mesh counter electrode, and a silver-foil pseudo reference. The spectroelectrochemical experiments were carried out in absolute acetonitrile containing 0.1 M Bu_4NPF_6 as the supporting electrolyte. The same solvents as for the CV measurements were used for each compound.

EPR Spectroscopy

EPR spectra at the X-band frequency (ca. 9.5 GHz) were obtained with a Magnetech MS-5000 benchtop EPR spectrometer equipped with a rectangular TE 102 cavity and a TC HO4 temperature controller. The measurements were carried out in synthetic quartz glass tubes. The low temperature EPR-spectra were performed up to −175 °C.

Calculations

The program package ORCA 4.1. was used for all DFT calculations.[45] Starting from the molecular structure obtained from X-ray diffraction geometry optimizations were carried out using the PBE0[46] functional and no symmetry restrictions were imposed during the optimization. All calculations were performed with empirical Van der Waals correction (D3).[47] The restricted and unrestricted DFT methods were employed for closed and open shell molecules respectively unless stated otherwise. Convergence criteria were set to default for geometry-optimization (OPT), and tight for SCF calculations (TIGHTSCF). Triple-ζ–valence basis sets (def2-TZVP)[48] were employed for all atoms. Calculations were performed using resolution of the identity approximation[49] with matching auxiliary basis sets[50] for geometry optimizations and numerical frequency calculations and the RIJCOSX (combination of the resolution of the identity and chain of spheres algorithms) approximation for single point calculations using the PBE0 functional.[46] Low-lying excitation energies were calculated with time-dependent DFT (TD-DFT). Solvent effects were taken into account with the conductor-like polarizable continuum model, CPCM.[51] Spin densities were calculated according to the Mulliken population analysis.[52] The absence of imaginary frequency Spin densities, molecular orbitals and difference densities were visualized with the modified Chemcraft 1.8 program.[53] All molecular orbitals are illustrated with an iso value of 0.052. All calculated TD-DFT spectra are Gaussian broadened with a band width of 25 at half height.

Synthesis and Characterization

Synthesis of [Rh(C–C)Cl](PF$_6$)

According to a modified synthetic procedure from Bolje *et al.*,[30] [H(**C**–**C**)](BF$_4$)[26] (0.87 g, 0.213 mmol), KCl (0.16 g, 2.125 mmol) and Ag_2O (0.17 g, 0.748 mmoL) was dissolved in 20 mL CH_3CN and stirred for 3 days at room temperature under exclusion of light. The solution was filtered and the remaining solvent was evaporated. [RhCp*Cl$_2$]$_2$ (0.07 g, 0.113 mmol) was added and dissolved in CH_2Cl_2. The reaction mixture was stirred for 3 days at room temperature under exclusion of light. An excess of KPF_6 (0.16 g, 0.850 mmol) was added and the reaction mixture was rigorous stirred for 20 min. The orange solution was filtered through Celite and extracted with 3 x H_2O (50 mL). The organic phase was separated and dried over Na_2SO_4. Additional crystallization from slow diffusion of *n*-hexane/Et_2O (1 : 1) into a concentrated solution of [Rh(**C**–**C**)Cl](PF$_6$) in CH_2Cl_2 yielded orange crystals (120 mg, 0.162 mmol, 77 %) suitable for X-ray diffraction analysis. In case of an insufficient conversion, purification by column chromatography (aluminum oxide, activated with 5 w% water; CH_2Cl_2/CH_3CN 100:0→1:1) resulted in pure [Rh(**C**–**C**)Cl](PF$_6$).

^{1}H NMR (500 MHz, $CDCl_3$) δ =8.77 (d, J=5.5 Hz, 1H), 8.10–8.03 (m, 2H), 7.59 (t, J=7.8 Hz, 1H), 7.54 (td, J=5.4, 2.8 Hz, 1H), 7.44 (dd, J=7.8, 1.1 Hz, 1H), 7.39 (dd, J=7.8, 1.1 Hz, 1H), 4.60 (s, 3H), 3.28 (hept, J=6.4 Hz, 1H), 2.58 (hept, J=6.4 Hz, 1H), 1.43 (s, 15H), 1.37 (d, J=6.6 Hz, 3H), 1.31 (d, J=6.6 Hz, 3H), 1.26 (d, J=6.6 Hz, 3H), 0.81 (d, J=6.9 Hz, 3H) ppm; **^{13}C{^{1}H} NMR** (126 MHz, $CDCl_3$) δ =170.31 (d, J=53.2 Hz, 1 C, MIC-Rh), 152.21, 148.45, 147.05, 146.66, 145.41, 139.34, 134.42, 131.72, 125.63, 125.63, 124.24, 124.05, 121.72, 97.72 (d, J=7.0 Hz, 5 C, Rh-Cp*), 39.22, 28.66, 27.88, 27.20, 25.55, 21.90, 21.80, 9.01 ppm; **MS (ESI-ToF)**: m/z found: 593.1944, calcd: 593.1913 ($C_{18}H_{22}ClN_4Rh^+$); **Elemental analysis** calcd. (%) for $C_{30}H_{39}ClF_6N_4PRh$: C 48.76, H 5.32, N 7.58; found: C 48.78, H 5.39, N 7.52.

Synthesis of [Rh(C–N)Cl](PF$_6$)

According to a modified synthetic procedure from Bolje *et al.*,[13] [H(**C**–**N**)](OTf)[15] (0.10 g, 0.213 mmol), KCl (0.16 g, 2.125 mmol) and Ag_2O (0.17 g, 0.748 mmoL) was dissolved in 20 mL CH_3CN and stirred for 3 days at room temperature under exclusion of light. The solution was filtered and the remaining solvent was evaporated. [RhCp*Cl$_2$]$_2$ (0.07 g, 0.113 mmol) was added and dissolved in CH_2Cl_2. The reaction mixture was stirred for 3 days at room temperature under exclusion of light. An excess of KPF_6 (0.16 g, 0.850 mmol) was added and the reaction mixture was rigorous stirred for 20 min. The orange solution was filtered through Celite and extracted with 3×H_2O (50 mL). The organic phase was separated and dried over Na_2SO_4. Additional crystallization from slow diffusion of *n*-hexane into a concentrated solution of [Rh(**C**–**N**)Cl](PF$_6$) in CH_2Cl_2 yielded orange crystals (142 mg, 0.192 mmol, 91 %) suitable for X-ray diffraction analysis. In case of an insufficient conversion, purification by column chromatography (aluminum oxide, activated with 5 w% water; CH_2Cl_2/CH_3CN 100:0→1:1) resulted in pure [Rh(**C**–**N**)Cl](PF$_6$). **^{1}H NMR** (500 MHz, $CDCl_3$) δ δ 8.67–8.64 (m, 1H), 8.27 (ddd, J=8.2, 1.3, 0.7 Hz, 1H), 8.19 (ddd, J=8.3, 7.6, 1.5 Hz, 1H), 7.73 (ddd, J=7.5, 5.6, 1.3 Hz, 1H), 7.60 (t, J=7.8 Hz, 1H), 7.42 (dd, J=7.9, 1.1 Hz, 1H), 7.38 (dd, J=7.8, 1.0 Hz, 1H), 4.01 (s, 3H), 3.09 (hept, J=6.7 Hz, 1H), 2.82 (hept, J=6.7 Hz, 1H), 1.55 (s, 12H), 1.37 (d, J=6.6 Hz, 2H), 1.29 (d, J=6.6 Hz, 2H), 1.25 (d, J=6.6 Hz, 2H), 0.86 (d, J=6.9 Hz, 2H) ppm; **^{13}C{^{1}H} NMR** (126 MHz, $CDCl_3$) δ =163.47 (d, J=49.7 Hz, 1 C, MIC-Rh), 151.07, 150.45, 150.32, 150.30, 145.69, 145.65, 141.60, 132.23, 127.24, 124.54, 124.13, 122.29, 115.54, 98.36 (d, J=7.2 Hz, 5 C, Rh-Cp*), 38.27, 30.55, 30.30, 25.49, 25.34, 24.55, 23.48, 9.45 ppm; **MS (ESI-ToF)**: m/z found: 593.1915, calcd: 593.1918 ($C_{18}H_{22}ClN_4Rh^+$); **Elemental analysis** calcd. (%) for $C_{30}H_{39}ClF_6N_4PRh$: C 48.76, H 5.32, N 7.58; found: C 48.32, H 5.48, N 7.20.

Synthesis of [Rh(C–C)MeCN](PF$_6$)$_2$

[Rh(**C**–**C**)Cl](PF$_6$) (0.03 g, 0.052 mmol) was dissolved in 3 mL CH_3CN and $AgPF_6$ (0.01 g, 0.057 mmol) was added. The reaction mixture was stirred overnight at room temperature under exclusion of light and filtered through Celite. The solvent was reduced to 1 mL and overlaid with Et_2O yielding yellow crystals of [Rh(**C**–**C**)MeCN](PF$_6$)$_2$ (0.04 g, 0.052 mmol, >99 %) suitable for X-ray diffraction analysis.

^{1}H NMR (250 MHz, CD_3CN) δ =8.93 (dd, J=5.6, 0.7 Hz, 1H), 8.31 (ddd, J=8.1, 7.6, 1.5 Hz, 1H), 8.22–8.15 (m, 1H), 7.85–7.76 (m, 1H),

7.71 (d, J=7.8 Hz, 1H), 7.56 (td, J=7.8, 1.2 Hz, 2H), 4.56 (s, 3H), 2.70 (hept, J=6.8 Hz, 1H), 2.47 (hept, J=6.8 Hz, 1H), 1.96 (s, 3H), 1.44 (s, 15H), 1.37 (d, J=6.7 Hz, 3H), 1.30 (d, J=6.6 Hz, 6H), 0.87 (d, J=6.8 Hz, 3H) ppm; **^{13}C{^{1}H} NMR** (63 MHz, CD_3CN) δ =166.98 (d, J=51.5 Hz, 1 C, Rh-MIC),154.76, 149.51, 147.66, 147.64, 147.32, 146.44, 142.01, 134.81, 133.52, 128.35, 128.35, 126.01, 125.74, 123.31, 123.30, 101.54 (d, J=7.3 Hz, 5 C, Rh-Cp*), 40.67, 29.82, 29.04, 27.45, 26.03, 22.16, 21.96, 9.64 ppm; **MS (ESI-ToF)**: m/z found: found: 593.1913, calcd: 593.1913 ($C_{30}H_{39}ClN_4Rh^+$); 557.2146, calcd: 557.2230 ($C_{30}H_{39}N_4Rh^+$); **Elemental analysis** calcd. (%) for $C_{32}H_{42}F_{12}N_4P_2Rh$: C 43.21, H 4.76, N 7.87; found: C 42.83, H 4.68, N 7.80.

Synthesis of [Rh(C–N)MeCN](PF$_6$)$_2$

[Rh(**C**–**N**)Cl](PF$_6$) (0.03 g, 0.052 mmol) was dissolved in 3 mL CH_3CN and $AgPF_6$ (0.01 g, 0.057 mmol) was added. The reaction mixture was stirred overnight at room temperature under exclusion of light and filtered through Celite. The solvent was reduced to 1 mL and overlaid with Et_2O yielding yellow crystals of [Rh(**C**–**N**)MeCN](PF$_6$)$_2$ (0.04 g, 0.052 mmol, >99%) suitable for X-ray diffraction analysis.

^{1}H NMR (700 MHz, CD_3CN) δ =8.82 (dd, J=5.6, 0.9 Hz, 1H), 8.45 (ddd, J=8.2, 7.7, 1.5 Hz, 1H), 8.33 (ddd, J=8.2, 1.3, 0.7 Hz, 1H), 7.93 (ddd, J=7.7, 5.6, 1.3 Hz, 1H), 7.73–7.69 (m, 1H), 7.55 (d, J=8.2 Hz, 1H), 7.51 (d, J=7.7 Hz, 1H), 4.06 (s, 3H), 2.70 (hept, J=6.6 Hz, 1H), 2.65 (hept, J=6.6 Hz, 1H), 1.96 (s, 2H), 1.53 (s, 15H), 1.36 (d, J=6.7 Hz, 3H), 1.30 (d, J=6.6 Hz, 3H), 1.25 (d, J=6.8 Hz, 3H), 0.94 (d, J=6.8 Hz, 3H) ppm; **^{13}C{^{1}H} NMR** (176 MHz, CD_3CN) δ =160.57 (d, J=48.3 Hz, 1 C, Rh-MIC), 152.86, 151.53, 150.95, 150.85, 147.41, 147.39, 144.70, 133.55, 138.39, 125,98, 125.98, 125.42, 122.36 166.36, 116.35, 101.97 (d, J=7.6 Hz, 5 C, Rh-Cp*), 39.72, 31.53, 31.40, 25.84, 25.63, 24.84, 23.67, 9.89 ppm; **MS (ESI-ToF)**: m/z found: 557.2158, calcd: 557.2230 ($C_{30}H_{39}N_4Rh^+$); **Elemental analysis** calcd. (%) for $C_{32}H_{42}F_{12}N_4P_2Rh$: C 43.21, H 4.76, N 7.87; found: C 43.03, H 4.68, N 7.80.

Synthesis of [Rh(C–C)H](PF$_6$)

[Rh(**C**–**C**)Cl](PF$_6$) (0.05 g, 0.087 mmol) was added in a 10 mL Schlenk-tube and rigorously stirred until a fine powder was formed. Subsequently, 3 mL of an aqueous NaOOCH/HCOOH (excess, pH= 4.8) was added and the fine suspension was refluxed at 85 °C overnight. The yellow suspension was filtered and washed extensively with degassed H_2O and dried overnight at 40 °C. The yellow solid was transferred in the synthetic glovebox and dissolved CD_3CN (for NMR) or THF (for crystallization) and filtered through a syringe filter. The THF solution was overlaid with *n*-hexane yielding crystalline material of [Rh(**C**–**C**)H](PF$_6$) (0.03 g, 0.035 mmol, 40% isolated yield, >98% NMR yield). Unfortunately, the obtained crystals were not suitable for X-ray diffraction analysis and all our attempts to obtain single crystals failed.

^{1}H NMR (500 MHz, CD_3CN) δ =8.74 (dq, J=5.7, 1.0 Hz, 1H), 8.09–8.05 (m, 2H), 7.64 (t, J=7.8 Hz, 1H), 7.52–7.48 (m, 2H), 7.45 (dd, J=7.8, 1.3 Hz, 1H), 4.49 (s, 3H), 2.73–2.65 (m, 1H), 2.67 (hept, J=6.8 Hz, 1H), 2.63 (hept, J=6.8 Hz, 1H), 1.56 (d, J=0.8 Hz, 15H, *through space coupling of Cp* with Hydride*), 1.39 (d, J=6.8 Hz, 3H), 1.32 (d, J=6.8 Hz, 3H), 1.24 (d, J=6.7 Hz, 3H), 0.89 (d, J=6.9 Hz, 3H), −11.46 (d, J=22.0 Hz, 1H) ppm; **^{13}C{^{1}H} NMR** (126 MHz, CD_3CN) δ (ppm) =155.19, 149.46, 147.57, 146.86, 143.30, 138.73, 135.48, 132.81, 125.70, 125.29, 125.17, 122,07, 98.42 (d, J=5.2 Hz, 5 C, Rh-Cp*), 40.07, 29.76, 29.40, 27.17, 25.63, 22.30, 22.28, 10.13 ppm; **MS (ESI-ToF)**: m/z found: 593.2301, calcd: 593.2303 ($C_{30}H_{40}N_4Rh^+$); 557.2135, calcd: 557.2230 ($C_{30}H_{39}N_4Rh^+$); **Elemental analysis** calcd. (%) for $C_{32}H_{42}F_{12}N_4P_2Rh$: C 51.14, H 5.72, N 7.98; found: C 49.90, H 5.64, N 7.56.

Note: The ^{1}H NMR shows no equilibrium with [Rh(**C**–**C**)]. Some traces of acidic impurities in the CD_3CN might shift the equilibrium to [Rh(**C**–**C**)H](PF$_6$).

Synthesis of [Rh(C–N)H](PF$_6$)

[Rh(**C**–**N**)Cl](PF$_6$) (0.05 g, 0.087 mmol) was added in a 10 mL Schlenk-tube and rigorously stirred until a fine powder was formed. Subsequently, 3 mL of an aqueous NaOOCH/HCOOH (excess, pH= 4.8) was added and the fine suspension was refluxed at 85 °C for two hours. The yellow suspension was filtered and washed extensively with degassed H_2O and dried overnight at 40 °C. The yellow solid was transferred in the synthetic glovebox and dissolved CD_3CN (for NMR) or THF (for crystallization) and filtered through a syringe filter. The THF solution was overlaid with *n*-hexane yielding yellow single crystals of [Rh(**C**–**N**)H](PF$_6$) suitable for X-ray diffraction analysis (0.03 g, 0.037 mmol, 43% isolated yield, >98% NMR yield).

^{1}H NMR (500 MHz, CD_3CN) δ =8.62 (d, J=5.6 Hz, 1H), 8.20 (d, J=3.8 Hz, 2H), 7.66–7.60 (m, 2H), 7.47 (d, J=7.9 Hz, 1H), 7.42 (d, J=7.8 Hz, 1H), 3.94 (s, 3H), 2.83 (hept, J=6.8 Hz, 1H), 2.58 (hept, J=6.9 Hz, 1H), 1.64 (d, J=0.8 Hz, 15H, *through space coupling of Cp* with Hydride*), 1.37 (d, J=6.7 Hz, 3H), 1.28 (d, J=6.7 Hz, 3H), 1.21 (d, J=6.7 Hz, 3H), 0.96 (d, J=6.9 Hz, 3H), −11.48 (d, J=23.1 Hz, 1H) ppm; **^{13}C{^{1}H} NMR** (126 MHz, CD_3CN) δ =168.72 (d, J=48.5 Hz, 1 C, Rh-MIC), 153.50, 151.53, 150.62, 150.60, 146.70, 146.65, 141.17, 132.80, 126.55, 125.12, 124.99, 123.87, 114.97, 98.77 (d, J=5.2 Hz, 5 C, Rh-Cp*), 39.00, 31.66, 31.56, 25.33, 24.97, 24.54, 24.34, 10.33 ppm; **MS (ESI-ToF)**: m/z found: 593.1985, calcd: 593.2303 ($C_{30}H_{40}N_4Rh^+$); 557.2185, calcd: 557.2230 ($C_{30}H_{39}N_4Rh^+$); **Elemental analysis** calcd. (%) for $C_{32}H_{42}F_{12}N_4P_2Rh$: C 51.14, H 5.72, N 7.98; found: C 51.04, H 5.79, N 7.65.

Note: The ^{1}H NMR shows no equilibrium with [Rh(**C**–**N**)]. Some traces of acidic impurities in the CD_3CN might shift the equilibrium to [Rh(**C**–**N**)H](PF$_6$).

Synthesis of [Rh(C–C)]

[Rh(**C**–**C**)Cl](PF$_6$) (0.05 g, 0.087 mmol) was dissolved in 5 mL THF and stored overnight at −40 °C. Upon addition of KC_8 (0.03 g, 0.182 mmol), the color changed immediately from orange to intense green. The reaction mixture was stirred for two hours at room temperature and filtered through a syringe filter. The solvent was evaporated and the crude product was dissolved in some drops of THF and *n*-hexane, filtered and stored at −40 °C for one month yielding a green solid (0.04 g, 0.068 mmol, 78%). Unfortunately, we were not able to isolate single crystals suitable for X-ray diffraction analysis in various solvents and different temperatures. The obtained ^{1}H and ^{13}C NMR spectrum was generated by addition of $NaBH_4$ to [Rh(**C**–**C**)H](PF$_6$) in CD_3CN at room temperature after one hour, since some reducing reagent was presented in the crude product (>98%, NMR yield).

^{1}H NMR (500 MHz, CD_3CN) δ =8.70 (dd, J=6.3, 1.0 Hz, 1H), 7.61–7.58 (m, 1H), 7.58–7.54 (m, 1H), 7.42 (d, J=7.8 Hz, 2H), 7.27–7.22 (m, 1H), 6.52 (td, J=6.5, 1.3 Hz, 1H), 4.43 (s, 3H), 2.69 (hept, J=6.8 Hz, 2H), 1.58 (s, 15H), 1.31 (d, J=6.9 Hz, 6H), 0.97 (d, J=6.8 Hz, 6H); **^{13}C{^{1}H} NMR** (126 MHz, CD_3CN) δ =150.53, 148.63, 146.15, 140.65, 137.64, 129.89, 123.27, 120.23, 118.95, 116.63, 89.74 (d, J=5.6 Hz, 5 C, Rh-Cp*), 37.63, 27.75, 23.70, 21.71, 9.12 ppm; **MS (ESI-ToF)**: m/z found: 559.2286, calcd: 559.2281 ($C_{30}H_{40}N_4Rh^+$).

Synthesis of [Rh(C–N)]

[Rh(**C**–**N**)Cl](PF$_6$) (0.05 g, 0.087 mmol) was dissolved in 5 mL THF and stored overnight at −40 °C. Upon addition of KC_8 (0.03 g, 0.182 mmol), the color changed immediately from orange to intense purple. The reaction mixture was stirred for two hours at room temperature and filtered through a syringe filter. The solvent was evaporated and the crude product was dissolved in some drops of THF and *n*-hexane, filtered and stored at −40 °C for one month yielding a purple crystal (0.01 g, 0.009 mmol, 10 %) suitable for X-ray diffraction analysis. The obtained ^{1}H NMR spectrum was generated by addition of $NaBH_4$ to [Rh(**C**–**N**)H](PF$_6$) in CD_3CN at room temperature after 10 minutes, since some reducing reagent was presented in the crystalline product (> 95 %, NMR yield). Unfortunately, we were not able to record a reasonable ^{13}C NMR.

^{1}H NMR (500 MHz, CD_3CN) δ =8.77 (dd, J=6.4, 0.7 Hz, 1H), 7.63 (d, J=8.2 Hz, 1H), 7.57–7.52 (m, 1H), 7.41 (d, J=7.7 Hz, 3H), 6.75 (td, J=6.8, 1.2 Hz, 1H), 3.61 (s, 3H), 2.81 (hept, J=6.6 Hz, 2H), 1.68 (s, 15H), 1.29 (d, J=6.8 Hz, 6H), 1.01 (d, J=6.9 Hz, 6H) ppm; **MS (ESI-ToF)**: m/z found: 279.1132, calcd: 279.6149 ($C_{30}H_{40}N_4Rh^{2+}$).

Performance of the Hydride Reactivity Experiments

Reactivity with $NaBH_4$: The respective [RhCp*] hydride complex was dissolved in CD_3CN and $NaBH_4$ was added at room temperature. The yellow reaction mixture changed rapidly to a deep purple (for [Rh(**C**–**N**)H](PF$_6$)) or dark green (for [Rh(**C**–**N**)H](PF$_6$)) solution under the evolution of gas. The reaction mixture was stirred for additional 10 min and transferred in a young NMR tube using a syringe filter.

Reactivity with TEMPO: The respective [RhCp*] hydride complex was dissolved in CH_3CN and TEMPO (approx. 0.9 eq.) (=(2,2,6,6-tetramethylpiperidin-1-yl)oxyl)) was added at room temperature. The reaction mixture was stirred until the TEMPO was completely dissolved and directly transferred in the EPR tube.

Reactivity with Tritylium: The respective [RhCp*] hydride complex was dissolved in CD_3CN and [(C_6H_5)$_3$C](PF$_6$) was added (> 1 eq). The reaction mixture was stirred for 10 min and transferred in a young NMR tube.

† Electronic supplementary information (ESI) available: Synthetic procedures, NMR spectra, X-ray crystallographic data, electrochemistry, spectroelectrochemistry, reactivity studies and computational details.

Acknowledgements

We thank Cindy Odenwald and Ivan Shestov for the synthetic support during their internship, Barbara Förtsch for elemental analyses, Dr. Wolfgang Frey (Institut für Organische Chemie) for collecting the X-ray data sets and the support by the state of Baden-Württemberg through bwHPC and the German Research Foundation (DFG) through grant no INST 40/575-1 FUGG (JUSTUS 2 cluster). Funded by the Deutsche Forschungsgemeinschaft [DFG, German Research Foundation – Project-IDs 358283783 – SFB 1333/2 2022. Open Access funding enabled and organized by Projekt DEAL.

Conflict of Interests

There are no conflicts to declare.

Data Availability Statement

The data that support the findings of this study are available in the supplementary material of this article.

Keywords: mesoionic carbenes · (spectro-)electrochemistry · RhCp* · ambiphilic hydride · precatalyst activation

[1] a) J. D. Blakemore, A. Gupta, J. J. Warren, B. S. Brunschwig, H. B. Gray, *J. Am. Chem. Soc.* **2013**, *135*, 18288; b) S. Cosnier, H. Gunther, *J. Electroanal. Chem.* **1991**, *315*, 307; c) N. Elgrishi, B. D. McCarthy, E. S. Rountree, J. L. Dempsey, *ACS Catal.* **2016**, *6*, 3644; d) R. Francke, B. Schille, M. Roemelt, *Chem. Rev.* **2018**, *118*, 4631; e) R. Ruppert, S. Herrmann, E. Steckhan, *Tetrahedron Lett.* **1987**, *28*, 6583; f) E. Steckhan, S. Herrmann, R. Ruppert, E. Dietz, M. Frede, E. Spika, *Organometallics* **1991**, *10*, 1568; g) T. K. Todorova, T. N. Huan, X. Wang, H. Agarwala, M. Fontecave, *Inorg. Chem.* **2019**, *58*, 6893; h) S. Enthaler, J. von Langermann, T. Schmidt, *Energy Environ. Sci.* **2010**, *3*, 1207; i) C. Finn, S. Schnittger, L. J. Yellowlees, J. B. Love, *Chem. Commun.* **2012**, *48*, 1392; j) E. E. Benson, C. P. Kubiak, A. J. Sathrum, J. M. Smieja, *Chem. Soc. Rev.* **2009**, *38*, 89; k) W.-H. Wang, Y. Himeda, J. T. Muckerman, G. F. Manbeck, E. Fujita, *Chem. Rev.* **2015**, *115*, 12936.
[2] S. Cosnier, A. Deronzier, N. Vlachopoulos, *J. Chem. Soc., Chem. Commun.* **1989**, *17*, 1259.
[3] S. Fukuzumi, T. Kobayashi, T. Suenobu, *ChemSusChem* **2008**, *1*, 827.
[4] W. Kaim, J. Fiedler, *Chem. Soc. Rev.* **2009**, *38*, 3373.
[5] D. A. Kurtz, J. L. Dempsey, *Inorg. Chem.* **2019**, *58*, 16510.
[6] J. A. Widegren, R. G. Finke, *J. Mol. Catal. A* **2003**, *198*, 317.
[7] V. Artero, M. Fontecave, *Chem. Soc. Rev.* **2013**, *42*, 2338.
[8] a) A. Jutand, *Chem. Rev.* **2008**, *108*, 2300; b) J. Liu, L. Lu, D. Wood, S. Lin, *ACS Cent. Sci.* **2020**, *6*, 1317.
[9] W. C. Henke, D. Lionetti, W. N. G. Moore, J. A. Hopkins, V. W. Day, J. D. Blakemore, *ChemSusChem* **2017**, *10*, 4589.
[10] J. A. Hopkins, D. Lionetti, V. W. Day, J. D. Blakemore, *Organometallics* **2019**, *38*, 1300.
[11] S. I. Johnson, H. B. Gray, J. D. Blakemore, W. A. Goddard, *Inorg. Chem.* **2017**, *56*, 11375.
[12] W. Kaim, R. Reinhardt, S. Greulich, J. Fiedler, *Organometallics* **2003**, *22*, 2240.
[13] U. Kölle, B.-S. Kang, P. Infelta, P. Comte, M. Grätzel, *Chem. Ber.* **1989**, *122*, 1869.
[14] Y. Peng, M. V. Ramos-Garcés, D. Lionetti, J. D. Blakemore, *Inorg. Chem.* **2017**, *56*, 10824.
[15] C. L. Pitman, O. N. L. Finster, A. J. M. Miller, *Chem. Commun.* **2016**, *52*, 9105.
[16] L. M. A. Quintana, S. I. Johnson, S. L. Corona, W. Villatoro, W. A. Goddard, M. K. Takase, D. G. VanderVelde, J. R. Winkler, H. B. Gray, J. D. Blakemore, *PNAS USA* **2016**, *113*, 6409.
[17] J. D. Blakemore, E. S. Hernandez, W. Sattler, B. M. Hunter, L. M. Henling, B. S. Brunschwig, H. B. Gray, *Polyhedron* **2014**, *84*, 14.
[18] U. Kölle, M. Grützel, *Angew. Chem. Int. Ed. Engl.* **1987**, *26*, 567.
[19] E. A. Boyd, D. Lionetti, W. C. Henke, V. W. Day, J. D. Blakemore, *Inorg. Chem.* **2019**, *58*, 3606.
[20] M. van der Meer, E. Glais, I. Siewert, B. Sarkar, *Angew. Chem.* **2015**, *127*, 13997.
[21] a) T. V. Q. Nguyen, W.-J. Yoo, S. Kobayashi, *Angew. Chem. Int. Ed. Engl.* **2015**, *54*, 9209; b) T. V. Q. Nguyen, W.-J. Yoo, S. Kobayashi, *Adv. Synth. Catal.* **2016**, *358*, 452; c) S. N. Sluijter, C. J. Elsevier, *Organometallics* **2014**, *33*, 6389; d) K. Farrell, H. Müller-Bunz, M. Albrecht, *Organometallics* **2015**, *34*, 5723.
[22] a) I. D. Alshakova, M. Albrecht, *ACS Catal.* **2021**, *11*, 8999; b) A. Bolje, S. Hohloch, M. van der Meer, J. Košmrlj, B. Sarkar, *Chem. Eur. J.* **2015**, *21*, 6756; c) R. Maity, A. Mekic, M. van der Meer, A. Verma, B. Sarkar, *Chem. Commun.* **2015**, *51*, 15106; d) Z. Mazloomi, R. Pretorius, O. Pàmies, M. Albrecht, M. Diéguez, *Inorg. Chem.* **2017**, *56*, 11282; e) Á. Vivancos, M.

Albrecht, *Organometallics* **2017**, *36*, 1580; f) Á. Vivancos, M. Beller, M. Albrecht, *ACS Catal.* **2018**, *8*, 17.
[23] a) F. Franco, M. F. Pinto, B. Royo, J. Lloret-Fillol, *Angew. Chem.* **2018**, *130*, 4693; b) T. Scherpf, C. R. Carr, L. J. Donnelly, Z. S. Dubrawski, B. S. Gelfand, W. E. Piers, *Inorg. Chem.* **2022**, *61*, 13644; c) F. Stein, M. Nößler, A. S. Hazari, L. Böser, R. Walter, H. Liu, E. Klemm, B. Sarkar, *Chem. Eur. J.* **2023**, *29*, e202300405; d) L. Suntrup, F. Stein, J. Klein, A. Wilting, F. G. L. Parlane, C. M. Brown, J. Fiedler, C. P. Berlinguette, I. Siewert, B. Sarkar, *Inorg. Chem.* **2020**, *59*, 4215.
[24] V. Ganesan, J. J. Kim, J. Shin, K. Park, S. Yoon, *Inorg. Chem.* **2022**, *61*, 5683.
[25] a) G. Guisado-Barrios, M. Soleilhavoup, G. Bertrand, *Acc. Chem. Res.* **2018**, *51*, 3236; b) R. Maity, B. Sarkar, *JACS Au* **2022**, *2*, 22; c) Á. Vivancos, C. Segarra, M. Albrecht, *Chem. Rev.* **2018**, *118*, 9493.
[26] L. Suntrup, S. Klenk, J. Klein, S. Sobottka, B. Sarkar, *Inorg. Chem.* **2017**, *56*, 5771.
[27] T. Bens, P. Boden, P. Di Martino-Fumo, J. Beerhues, U. Albold, S. Sobottka, N. I. Neuman, M. Gerhards, B. Sarkar, *Inorg. Chem.* **2020**, *59*, 15504.
[28] C. W. Machan, *Curr. Opin. Electrochem.* **2019**, *15*, 42.
[29] C. W. Machan, M. D. Sampson, S. A. Chabolla, T. Dang, C. P. Kubiak, *Organometallics* **2014**, *33*, 4550.
[30] A. Bolje, S. Hohloch, D. Urankar, A. Pevec, M. Gazvoda, B. Sarkar, J. Košmrlj, *Organometallics* **2014**, *33*, 2588.
[31] C. White, A. Yates, P. M. Maitlis, *Inorg. Synth.* **29**, *1992*, 228.
[32] M. L. Clark, K. A. Grice, C. E. Moore, A. L. Rheingold, C. P. Kubiak, *Chem. Sci.* **2014**, *5*, 1894.
[33] a) M. Poyatos, E. Mas-Marzá, J. A. Mata, M. Sanaú, E. Peris, *Eur. J. Inorg. Chem.* **2003**, *2003*, 1215; b) M. Poyatos, W. McNamara, C. Incarvito, E. Clot, E. Peris, R. H. Crabtree, *Organometallics* **2008**, *27*, 2128; c) M. Poyatos, M. Sanaú, E. Peris, *Inorg. Chem.* **2003**, *42*, 2572.
[34] L. Dadci, H. Elias, U. Frey, A. Hoernig, U. Koelle, A. E. Merbach, H. Paulus, J. S. Schneider, *Inorg. Chem.* **1995**, *34*, 306.
[35] a) C. Caix, S. Chardon-Noblat, A. Deronzier, J.-C. Moutet, S. Tingry, *J. Organomet. Chem.* **1997**, *540*, 105; b) K. M. Waldie, F. M. Brunner, C. P. Kubiak, *ACS Sustainable Chem. Eng.* **2018**, *6*, 6841.
[36] Y. Hu, J. R. Norton, *J. Am. Chem. Soc.* **2014**, *136*, 5938.
[37] W. C. Henke, Y. Peng, A. A. Meier, E. Fujita, D. C. Grills, D. E. Polyansky, J. D. Blakemore, *PNAS USA* **2023**, *120*, e2217189120.
[38] D. A. Smith, D. E. Herbert, J. R. Walensky, O. V. Ozerov, *Organometallics* **2013**, *32*, 2050.
[39] K. M. Waldie, A. L. Ostericher, M. H. Reineke, A. F. Sasayama, C. P. Kubiak, *ACS Catal.* **2018**, *8*, 1313.
[40] T. Bens, R. R. M. Walter, J. Beerhues, M. Schmitt, I. Krossing, B. Sarkar, *Chem. Eur. J.* **2023**, *29*, e202301205.
[41] a) S. Hammes-Schiffer, *Acc. Chem. Res.* **2001**, *34*, 273; b) S. Hammes-Schiffer, A. V. Soudackov, *J. Phys. Chem. B* **2008**, *112*, 14108; c) J. J. Warren, T. A. Tronic, J. M. Mayer, *Chem. Rev.* **2010**, *110*, 6961; d) D. R. Weinberg, C. J. Gagliardi, J. F. Hull, C. F. Murphy, C. A. Kent, B. C. Westlake, A. Paul, D. H. Ess, D. G. McCafferty, T. J. Meyer, *Chem. Rev.* **2012**, *112*, 4016.
[42] S. Budavari, *An encyclopedia of chemicals, drugs, and biologicals*, (Ed.) The Merck index., Merck, Rahway, N.J., U.S.A., **1991**.
[43] a) *APEX3*, Bruker AXS Inc, Madison, Wisconsin, USA, **2015**; b) C. F. Macrae, P. R. Edgington, P. McCabe, E. Pidcock, G. P. Shields, R. Taylor, M. Towler, J. van de Streek, *J. Appl. Crystallogr.* **2006**, *39*, 453; c) SAINT+, *Data Integration Engine*, Bruker AXS Inc., Madison, Wisconsin, USA, 1997–2012, v. 8.27b©; d) G. M. Sheldrick, *SHELXS-97 and SHELXL-97, Program for Crystal Structure Solution and Refinement*, University of Gottingen, Göttingen, Germany, **1997**; e) G. M. Sheldrick, *Program for Empirical Absorption Correction*, University of Göttingen, Göttingen, Germany, **2008**; f) G. M. Sheldrick, *Program for Crystal Structure Solution and Refinement*, University of Göttingen, Göttingen, Germany, **2014**; g) G. M. Sheldrick, *Acta Crystallogr.* **2008**, *A64*, 112; h) G. M. Sheldrick, *Acta Crystallogr.* **2015**, *C71*, 3.
[44] a) J. Klein, A. Stuckmann, S. Sobottka, L. Suntrup, M. van der Meer, P. Hommes, H.-U. Reissig, B. Sarkar, *Chem. Eur. J.* **2017**, *23*, 12314; b) M. Krejčik, M. Daněk, F. Hartl, *J. Electroanal. Chem.* **1991**, *317*, 179.
[45] F. Neese, *Comput. Mol. Sci.* **2012**, *2*, 73.
[46] C. Adamo, V. Barone, *J. Chem. Phys.* **1999**, *110*, 6158.
[47] a) S. Grimme, *J. Comput. Chem.* **2004**, *25*, 1463; b) S. Grimme, *J. Comput. Chem.* **2006**, *27*, 1787; c) S. Grimme, J. Antony, S. Ehrlich, H. Krieg, *J. Chem. Phys.* **2010**, *132*, 154104; d) S. Grimme, S. Ehrlich, L. Goerigk, *J. Comput. Chem.* **2011**, *32*, 1456.
[48] F. Weigend, R. Ahlrichs, *Phys. Chem. Chem. Phys.* **2005**, *7*, 3297.
[49] a) R. Izsák, F. Neese, *J. Chem. Phys.* **2011**, *135*, 144105; b) F. Neese, *J. Comput. Chem.* **2003**, *24*, 1740; c) F. Neese, G. Olbrich, *Chem. Phys. Lett.* **2002**, *362*, 170; d) F. Neese, F. Wennmohs, A. Hansen, U. Becker, *Chem. Phys.* **2009**, *356*, 98; e) T. Petrenko, S. Kossmann, F. Neese, *J. Chem. Phys.* **2011**, *134*, 54116; f) O. Vahtras, J. Almlöf, M. W. Feyereisen, *Chem. Phys. Lett.* **1993**, *213*, 514; g) J. L. Whitten, *J. Chem. Phys.* **1973**, *58*, 4496.
[50] a) K. Eichkorn, O. Treutler, H. Öhm, M. Häser, R. Ahlrichs, *Chem. Phys. Lett.* **1995**, *242*, 652; b) K. Eichkorn, F. Weigend, O. Treutler, R. Ahlrichs, *Theor. Chem. Acc.* **1997**, *97*, 119.
[51] V. Barone, M. Cossi, *J. Phys. Chem. A* **1998**, *102*, 1995.
[52] R. S. Mulliken, *J. Chem. Phys.* **1955**, *23*, 1833.
[53] G. A. Zhurko, *Chemcraft-Graphical Program for Visualization of Quantum Chemistry Computations*, Ivanovo, Russia, **2023**.

Manuscript received: July 24, 2023
Accepted manuscript online: September 28, 2023
Version of record online: November 20, 2023